



1 **Glacial erosion and history of Inglefield Land, northwest** 2 **Greenland**

3

4

5

6 Caleb K. Walcott-George¹, Allie Balter-Kennedy², Jason P. Briner¹, Joerg M. Schaefer², Nicolás
7 E. Young²

8

9 ¹Department of Geology, University at Buffalo, Buffalo, NY 14260, USA

10 ²Lamont-Doherty Earth Observatory, Columbia University, Palisades, NY 10964, USA

11

12 *Correspondence to:* Caleb Walcott-George (ckwalcot@buffalo.edu)

13 **Abstract:**

14 We used mapping of bedrock lithology, bedrock fractures, and lake density in Inglefield Land,
15 northwest Greenland, combined with cosmogenic nuclide (¹⁰Be and ²⁶Al) measurements in
16 bedrock surfaces, to investigate glacial erosion and the ice-sheet history of the northwestern
17 Greenland Ice Sheet. The pattern of eroded versus weathered bedrock surfaces and other glacial
18 erosion indicators reveal temporally and spatially varying erosion under cold- and warm-based ice.
19 All of the bedrock surfaces that we measured in Inglefield Land contain cosmogenic nuclide
20 inheritance with apparent ¹⁰Be ages ranging from 24.9 ± 0.5 to 215.8 ± 7.4 ka. The ²⁶Al/¹⁰Be ratios
21 require minimum surface histories of ~150 to 2000 kyr. Because our sample sites span a relatively
22 small area that experienced a similar ice-sheet history, we attribute differences in nuclide
23 concentrations and ratios to varying erosion during the Quaternary. We show that an ice sheet
24 history with ~900 kyr of exposure and ~1800 kyr of ice cover throughout the Quaternary is
25 consistent with the measured nuclide concentrations in most samples when sample-specific
26 subaerial erosion rates are between 0 and 2 × 10⁻² mm yr⁻¹ and subglacial erosion rates are between
27 0 and 2 × 10⁻³ mm yr⁻¹. These erosion rates help to characterize arctic landscape evolution in
28 crystalline bedrock terrains in areas away from focused ice flow.



29 **1. Introduction**

30

31 The Greenland Ice Sheet is presently the largest single contributor to sea-level rise and is predicted
32 to continue to melt at an accelerated rate throughout the next century (e.g., Aschwanden and
33 Brinkerhoff, 2022; Goelzer et al., 2020). Ice streams play a large role in modulating the volume of
34 the modern Greenland Ice Sheet, and their stability is directly linked to overall ice sheet mass
35 balance (e.g., Khan et al., 2022; Mouginot et al., 2015). These features are large areas of fast-
36 moving ice, with onset zones that feed into main channels, which eventually calve into the ocean
37 and are constrained by topography or slow-moving ice (Benn and Evans, 2010).

38 Ice sheet models used to predict future ice sheet evolution are aided by the knowledge of
39 long-term ice sheet history and patterns of past ice flow variability, as these play a large role in
40 modulating ice sheet mass balance (e.g., Hubbard et al., 2009). Uncertainty in ice-sheet model
41 parameters can be narrowed when paleo-ice-sheet simulations are performed alongside geologic
42 constraints (e.g., Briner et al., 2020; Cuzzone et al., 2016; Patton et al., 2017). Observations of
43 many ice-sheet processes are sparse because it is difficult to access the bed of modern ice sheets;
44 thus, investigating the beds of former ice sheets (i.e., previously glaciated landscapes) provides
45 information on past ice sheet dynamics and basal processes.

46 The distribution of glacial erosional features across formerly glaciated landscapes has been
47 used to map past basal thermal conditions and relative ice velocities delineating zones of warm-
48 bedded and/or fast flowing ice where erosional features are abundant, from areas of cold-based ice
49 and ancient landscape preservation where these features are absent (Andrews et al., 1985; Daly,
50 1902; Flint, 1943; Margold et al., 2015; Sugden, 1978). Identifying areas of differential erosion in
51 formerly glaciated landscapes is particularly useful for mapping paleo-ice streams, as knowing
52 their extent is helpful for understanding the mass balance of former ice sheets through ice sheet



53 models. Paleo-ice stream onset zones are found at the transitions between warm-and cold-based
54 ice, which can be delineated via mapping of erosion imprints on a landscape and cosmogenic
55 nuclide analysis (Briner et al., 2008; Margold et al., 2015, 2018)

56 Cosmogenic nuclides are produced mostly in the upper few meters of the Earth's surface
57 when it is exposed to the cosmic ray flux and are routinely used in formerly glaciated landscapes
58 to quantify erosion rates and the timing of past ice sheet fluctuations (Gosse and Phillips, 2001).
59 In areas covered by warm-based, highly erosive glaciers, nuclides that have accumulated in the
60 upper 2-3 meters of bedrock are often removed through efficient glacial erosion. In areas of
61 minimal-to-no glacial erosion (i.e., covered by cold-bedded glaciers or short-lived erosive ice),
62 bedrock surfaces contain inventories of cosmogenic nuclides from multiple periods of exposure
63 (known as cosmogenic nuclide inheritance; Bierman et al., 1999). Patterns of inheritance (or lack
64 thereof) across a landscape can be used to delineate ice streaming where faster flowing, erosive
65 ice depleted nuclide inventories (Briner et al., 2006; Corbett et al., 2013; Roberts et al., 2013).

66 Cosmogenic nuclide inheritance resulting from minimal glacial erosion can pose an issue
67 for single nuclide surface exposure dating, where the apparent exposure age will be anomalously
68 old (Ivy-Ochs and Briner, 2014). However, some cosmogenic nuclides are radioactive and decay
69 when they are shielded from the cosmic ray flux by ice (e.g., ^{10}Be , ^{26}Al , and *in-situ* ^{14}C). The
70 production ratio of $^{26}\text{Al}/^{10}\text{Be}$ is 7.3:1 in quartz at the Earth's surface across Greenland (Corbett et
71 al., 2017). Because ^{26}Al has a shorter half-life (705 kyr) than ^{10}Be (1388 kyr), departure from this
72 ratio indicates surface burial (Korschinek et al., 2010; Nishiizumi, 2004). By measuring multiple
73 nuclides in bedrock surfaces near the modern Greenland Ice Sheet margin, researchers have
74 exploited cosmogenic nuclide inheritance to investigate periods of ice sheet minima, glacial



75 erosion, and longer-term ice sheet history (e.g., Corbett et al., 2013; Skov et al., 2020; Young et
76 al., 2021).

77 Recently, attention has been drawn to retrieving samples from the bed of extant ice sheets
78 (Briner et al., 2022; Johnson et al., 2024; Spector et al., 2018). The information contained at the
79 contemporary ice-bed interface provides valuable, and rare, terrestrial constraints on previous ice
80 sheet minima and long-term ice sheet history. Cosmogenic nuclide and luminescence analysis of
81 sediment and bedrock samples collected from this key transition zone under ice sheets have
82 provided insight into the stability of the ice sheet throughout the Quaternary (Balco et al., 2023;
83 Bierman et al., 2023; Christ et al., 2020; Christ et al., 2021; Christ et al., 2023; Schaefer et al.,
84 2016). Studying the landscape at the fringes of the Greenland Ice Sheet allows us to systematically
85 investigate large areas of the former ice sheet bed, without the need to drill through the ice sheet,
86 providing complementary results for efforts focused on obtaining material from under the ice.

87 We mapped bedrock features and used cosmogenic nuclide analysis to determine the extent
88 and magnitude of erosion and the ice sheet history across Inglefield Land, northwest Greenland
89 over the Quaternary. We established that while most of Inglefield Land was covered by cold-based
90 ice during the last glacial cycle, there were areas of ice streaming in incised valleys near the modern
91 coastline. Finally, we modeled cosmogenic nuclide accumulation through the Quaternary glacial
92 cycles and find that our measurements are consistent with an ice-sheet history with 900 kyr of
93 cumulative exposure and 1800 kyr of cumulative ice cover when we allowed subaerial and
94 subglacial erosion rates to vary for each sample.

95

96

97



98 2. Inglefield Land

99 Inglefield Land is an ice-free area in northwest Greenland situated between the Greenland Ice
100 Sheet and the coastline 30 km to the northwest. It is bounded by Smith Sound to the west, Kane
101 Basin to the north, Prudhoe Dome and the main body of the northern Greenland Ice Sheet to the
102 south, and the Hiawatha Glacier sector of the Greenland Ice Sheet to the east (Fig. 1). Today, much
103 of the ice bordering Inglefield Land is cold based (MacGregor et al., 2022). Inglefield Land is
104 characterized by relatively low-relief uplands that reach 700 m asl near the ice margin with valleys
105 incised along the northern coast. Ice sheet meltwater drains into through these valleys and into four
106 embayments (from west to east): Force Bay, Rensselaer Bay, Dallas Bay, and Marshall Bay
107 (henceforth the unnamed valleys crossing Inglefield Land will be referred to by the bays into which
108 they drain).

109 During the Last Glacial Maximum (LGM; 26 – 19 ka), the northern Greenland Ice Sheet
110 covered Inglefield Land completely as it advanced into Kane Basin, where it coalesced with the
111 Innuitian Ice Sheet and flowed southward, eventually terminating in an iceshelf spanning northern
112 Baffin Bay (Fig. 1; England, 1999; Couette et al., 2022; Batchelor et al., 2024). Although the
113 timing and duration of the LGM ice advance remains unknown, retreat onto the modern coast of
114 Inglefield Land is constrained to ~8.6 – 7.9 ka based on radiocarbon dating of organic material in
115 raised beach deposits and *in-situ* ¹⁴C ages from erratic boulders (Blake et al., 1992; Mason, 2010;
116 Nichols, 1969; Søndergaard et al., 2020). The ice sheet continued to decay, arriving at the modern
117 margin by ~7 ka and maintaining to a smaller-than-modern position between ~5.8 and 0.3 ka, an
118 estimate based on radiocarbon ages from reworked wood fragments at the modern ice margin
119 (Søndergaard et al., 2020).



120 The pre-Holocene ice-sheet history and dynamics of Inglefield Land is not known, though
121 cosmogenic nuclide inheritance found in boulders across Inglefield Land indicates that much of
122 the landscape was covered by cold-based ice during the last glacial cycle (Søndergaard et al.,
123 2020). Limited ice sheet-scale terrestrial records suggest that there were major deglaciation events
124 during the Quaternary as captured by cosmogenic nuclide and luminescence analysis of sub-ice
125 sediment and bedrock at Camp Century and Summit, during which Inglefield Land was almost
126 certainly ice free (Christ et al., 2021; Christ et al., 2023; Schaefer et al., 2016). Additionally,
127 offshore marine sediment records imply that the ice sheet underwent several cycles of advance and
128 retreat, though inland extent of ice-sheet recession in North Greenland during interglacials is
129 poorly constrained (Bierman et al., 2016; Colville et al., 2011; Hatfield et al., 2016; Knutz et al.,
130 2019; Reyes et al., 2014).

131
132
133
134
135
136
137
138
139
140
141
142
143
144
145
146



147 **3 Methods**

148 We used mapping, field observations, ^{10}Be and ^{26}Al measurements from bedrock surfaces at eleven
149 sites to assess the ice sheet history and erosive conditions of the northwestern Greenland Ice Sheet
150 across Inglefield Land. Mapping and field observations allowed us to broadly identify variable
151 erosion across the landscape, while cosmogenic nuclide measurements helped us quantify ice-
152 sheet history and erosion.

153

154 ***3.1 Geologic mapping – GIS and field observations***

155 ***3.1.1 Bedrock lithology***

156 The relatively simple bedrock geology of Inglefield Land allowed us to investigate the long-term
157 pattern of erosion and landscape evolution of the area using pre-existing geologic maps. Inglefield
158 Land is underlain by crystalline paragneiss and capped with near-horizontally bedded sedimentary
159 rocks; therefore, generally speaking, outcrops of basement rock indicate areas where cap rocks
160 have been removed by erosion (Fig. 2). Some of this cap rock removal likely took place prior to
161 Quaternary glaciation (e.g., Krabbendam and Bradwell, 2014), but the patterns seen in the geologic
162 map – with crystalline lithologies in glacial troughs – hints at the role of past glacial erosion in
163 shaping the landscape. To identify the removal of sedimentary cap rocks, we created a simplified
164 geologic map of Inglefield Land using the 1:500,000 Greenland-wide geologic map in ArcGIS Pro
165 (Kokfelt et al., 2023) and classified units as crystalline, sedimentary, Quaternary sediments or
166 lakes. In the field, we noted the lithology at each of our sample sites and the relative amount of
167 weathering or ice sculpting (Figs. 2, 3).

168

169



170 *3.3.2 Mapping bedrock fractures*

171 Bedrock fractures in glaciated terranes are exposed through the removal of regolith by glacial
172 erosion (Gordon, 1981; Skyttä et al., 2023; Sugden, 1974, 1978). Areas with a high density of
173 exposed bedrock fractures within crystalline bedrock terranes have been used to identify intense
174 glacial erosion (e.g., Sugden, 1978). This is in contrast to areas where bedrock fractures are
175 obscured by sediment cover, a regolith mantle, or in some cases, sub-horizontal sedimentary
176 bedrock units. Our field area has a heterogenous pattern of mappable fractures that are easily
177 identifiable at the landscape-level, indicative of areas where regolith has been stripped via glacial
178 erosion. We outlined zones of bedrock fractures at the landscape scale in ArcGIS Pro using a 25
179 m resolution digital elevation model (Korsgaard et al., 2016). We created hillshade images with a
180 three-times vertical exaggeration for our mapping (Fig. 4). Our digital elevation model resolution
181 of 25 m was fine enough to capture areas of obvious bedrock fractures on a landscape scale, but
182 coarse enough to avoid issues with differentiating fractures from other features.

183

184 *3.3.3 Mapping lake density*

185 Lake density has also been used as a proxy for glacial erosion (e.g., Andrews et al., 1985; Briner
186 et al., 2008; Sugden, 1978). Areas of regolith cover are generally smooth on the landscape-scale
187 and contain few lakes. Meanwhile, erosive ice sheets can remove this overlying regolith and
188 expose the underlying bedrock, after which the bedrock is susceptible to ice sheet scouring and
189 erosion. These bedrock basins then fill with water following glacial retreat forming lakes across
190 previously-glaciated areas and thus, the density of lakes can be used as an indicator of past ice
191 sheet erosion. We created an inventory of lakes in Inglefield Land to calculate lake density (Fig.
192 5). While the 1:500,000 geologic map of Greenland shows larger lakes, smaller lakes are not



193 included due to the relatively coarse map resolution (Kokfelt et al., 2023). Therefore, we used a
194 semi-automated process in ArcGIS Pro to map all lakes in the study area. First, we used cloud-free
195 LANDSAT8 images to visualize surface water (Band 1; visible blue-green). We explored a range
196 of threshold values to extract cells with surface water from this image (i.e., cells with a value
197 higher than the threshold were water) and evaluated these against the original LANDSAT8 images
198 to determine a suitable threshold value that adequately captured lakes and streams. We converted
199 this raster to polygons of lake and river extents. Finally, we conducted manual quality control by
200 removing rivers and any lakes that were either dammed by sediments or the ice sheet and then
201 merged our new lake polygons with those from the geologic map. To calculate lake density across
202 Inglefield Land, we determined the percentage of each cell in a 1 x 1 km grid covered by lake
203 polygons.

204

205 ***3.4 Cosmogenic nuclide measurements***

206 *3.4.1 Sampling approach*

207 We collected samples for cosmogenic nuclide measurements from bedrock surfaces along two
208 SSE – NNW transects from the ice margin to the coast in Inglefield Land (Figs. 1 – 5). We sampled
209 roughly one kg of crystalline rock from 15 bedrock surfaces and one boulder using a handheld
210 angle grinder, hammer, and chisel during summer 2022. We collected nine samples along our
211 western transect (beginning at the mouth of Rensselaer Valley): two from bedrock surfaces and
212 one from a boulder (2.5 m long x 1.6 m wide x 1.1 m tall) close to the ice margin, one bedrock
213 sample from each of three separate inland sites, one bedrock sample from a higher-elevation
214 coastal site (255 m asl), and two bedrock samples from a lower-elevation coastal site (~100 m asl).
215 Along our eastern transect (beginning at the mouth of western Marshall Valley), we collected



216 bedrock samples: three from near the ice margin, one sample from each of three different inland
217 sites, and one sample from a low-elevation coastal site (~100 m asl).

218

219

220 *3.4.2 Lab procedures*

221 We measured ^{10}Be and ^{26}Al in all 16 of our samples. We isolated quartz and extracted ^{10}Be and
222 ^{26}Al at the University at Buffalo Cosmogenic Isotope Laboratory ($n = 12$) and the Lamont-Doherty
223 Earth Observatory (LDEO) cosmogenic dating laboratory ($n = 4$) using well-established
224 procedures (Corbett et al., 2016b; Kohl and Nishiizumi, 1992). We spiked our dissolved samples
225 with precisely weighed ^9Be carrier (PRIME Lab 2017.11.17-Be #3/#4 – ^9Be concentration of 1074
226 ± 8 ppm – at the University at Buffalo and LDEO carrier – ^9Be concentration of 1038.8 ppm – at
227 LDEO). We measured the amount of native ^{27}Al in our dissolved quartz and added varying
228 amounts of ^{27}Al carrier to ensure each sample had ~2000 mg of ^{27}Al . We measured the total amount
229 of ^{27}Al in aliquots removed after sample digestion with inductively coupled plasma optical
230 emission spectrometry. We sent ^{10}Be samples processed at the University at Buffalo and all ^{26}Al
231 samples to PRIME Lab and ^{10}Be samples processed at Lamont-Doherty to Lawrence-Livermore
232 National Laboratory, where the $^{10}\text{Be}/^9\text{Be}$ and $^{26}\text{Al}/^{27}\text{Al}$ ratios were measured by accelerator mass
233 spectrometry.

234 $^{10}\text{Be}/^9\text{Be}$ ratios were measured relative to the 07KNSTD standard ($^{10}\text{Be}/^9\text{Be}$ ratio: $2.85 \times$
235 10^{-12} ; Nishiizumi et al., 2007) at both facilities and ^{26}Al samples relative to the KNSTD standard
236 ($^{26}\text{Al}/^{27}\text{Al}$ ratio: 1.82×10^{-12} ; Nishiizumi, 2004). Analytical uncertainties (1σ) of ^{10}Be
237 measurements at Lawrence Livermore were between 1.8% and 1.9% and ranged from 1.5% to
238 6.0%, with an average of $2.6 \pm 1.3\%$ at PRIME lab. ^{26}Al measurement uncertainties ranged from



239 3.6% to 8.4% with an average of $4.8 \pm 1.5\%$. We applied background corrections to both ^{10}Be and
240 ^{26}Al sample ratios using batch-specific process blank values (Table S1).

241 We calculated apparent exposure ages using version 3 of the online exposure age calculator
242 from Balco et al. (2008). We used the Arctic ^{10}Be production rate, with a time-independent ‘St’
243 production rate scaling method to calculate apparent exposure ages (Lal, 1991; Stone, 2000; Young
244 et al., 2013). We did not include production rate uncertainties in our exposure age calculations
245 because we do not compare our age results to other independent dating methods. We used a
246 Greenland-specific $^{26}\text{Al}/^{10}\text{Be}$ surface production ratio in quartz of 7.3 for interpreting
247 exposure/burial histories from both nuclides (Corbett et al., 2017).

248

249

250

251

252

253

254

255 ***3.5 Modeling cosmogenic nuclide accumulation in rock surfaces***

256 In bedrock samples with cosmogenic nuclide inheritance, measurements of two isotopes with
257 different half-lives have been used to calculate Greenland Ice Sheet exposure and burial histories
258 (e.g. Andersen et al., 2020; Beel et al., 2016; Corbett et al., 2013; Knudsen and Egholm, 2018;
259 Knudsen et al., 2015; Skov et al., 2020; Strunk et al., 2017). Although *in-situ* ^{14}C ages constrain
260 ice retreat across Inglefield Land to between ~ 9 and 7 ka, apparent ^{10}Be ages date from boulders
261 date to between 8.3 ± 1.2 and 92.7 ± 1.5 ka, indicating the presence of nuclide inheritance



262 (Søndergaard et al., 2020). Inglefield Land bedrock also is likely to contain nuclide inheritance
263 and therefore yield information about ice sheet history and erosion prior to the last glacial cycle.
264 Given the relatively small distance from the modern ice margin to coast and the speed at which
265 Inglefield Land deglaciated following the LGM, we hypothesize that, within ^{10}Be and ^{26}Al
266 measurement uncertainties, the 15 bedrock samples should have similar ice-cover histories on
267 glacial-interglacial timescales. Therefore, differences in ^{10}Be and ^{26}Al concentrations across the
268 landscape likely relate to varying sample-to-sample sub-glacial and sub-aerial erosion rates and
269 not differences in ice-sheet history at each sample location..

270 To explore this hypothesis, we simulate complex Pleistocene exposure histories using a
271 forward model that calculates cosmogenic ^{10}Be and ^{26}Al accumulation in rock brought to the
272 Earth's surface by subaerial and subglacial erosion. Because little is known about the ice-margin
273 history in Inglefield Land prior to the Holocene, we define the pre-Holocene exposure/burial
274 history by applying a threshold value on the benthic $\delta^{18}\text{O}$ LR04 stack (Lisiecki and Raymo,
275 2005) to define a range of plausible exposure/burial scenarios for the last 2.7 Myr, following the
276 approach adopted in prior studies (Balter-Kennedy et al., 2021; Knudsen et al., 2015). Exposure
277 and burial take place at $\delta^{18}\text{O}$ values below and above the threshold, respectively. We use a 30 kyr
278 running mean to smooth the $\delta^{18}\text{O}$ curve (Knudsen et al., 2015). . Given the prevalence of nuclide
279 inheritance across Inglefield Land (Søndergaard et al., 2020), we do not expect ^{10}Be to give post-
280 LGM deglaciation ages at each sample location, but deglaciation ages from *in situ* ^{14}C in boulders
281 at the coast and ice margin are provided by Søndergaard et al. (2020). We therefore estimate site-
282 specific Holocene exposure durations by scaling the deglaciation ages from Søndergaard et al.
283 (2020) to each of our sites based on their relative distance between the coast and ice margin, as
284 calculated along our sample transects.



285 The cosmogenic-nuclide concentration (atoms g⁻¹), N , for nuclide, i , at the end of each
286 timestep, j , is the sum of nuclides inherited from the previous timestep (adjusted for radioactive
287 decay) and the new accumulation of nuclides (assumed zero when ice covered and limited by the
288 surface erosion rate when ice free):

289

290

$$N_{i,j} = N_{i,j-1}e^{-\lambda_i t_j} + \int_0^{t_j} P_i(z_{end,j} + \varepsilon_j \tau) e^{-\lambda_i \tau} d\tau$$

291

292 where λ is the decay constant (5.00×10^{-7} for ¹⁰Be; 9.83×10^{-7} for ²⁶Al; (Korschinek et al., 2010;
293 Nishiizumi, 2004) and t_j is the duration of the timestep (yrs). P_i is the sum of nuclide production
294 (atoms g⁻¹ yr⁻¹) by spallation and muon interactions at a given mass depth (g cm⁻²). Here, mass
295 depth is time-varying, controlled by subaerial and subglacial erosion during ice-free and ice-
296 covered timesteps, respectively. Therefore, the mass depth is defined by the sample depth at the
297 end of each timestep, $z_{end,j}$, and the erosion rate (g cm⁻² yr⁻¹), ε_j , during that timestep. We calculate
298 spallation production rates at the Earth's surface using the Arctic ¹⁰Be calibration dataset of Young
299 et al. (2013), a ²⁶Al/¹⁰Be ratio of 7.3 (Corbett et al., 2017; Young et al., 2021), and the scaling
300 method of Stone (2000). We assume spallation production decreases exponentially with mass
301 depth at an attenuation length of 160 g cm⁻². We calculate production by muon interactions in
302 MATLAB using the cross sections for ¹⁰Be and ²⁶Al determined by Balco (2017) and implemented
303 in Model 1A in the same reference.

304 We determine the misfit between the modeled and measured nuclide concentrations for
305 each sample, d , using the error-weighted sum of squares (EWSS):

306

$$EWSS = \left(\frac{N_{10,p,d} - N_{10,m,d}}{\sigma_{10,m,d}} \right)^2 + \left(\frac{N_{26,p,d} - N_{26,m,d}}{\sigma_{26,m,d}} \right)^2$$

307



308 where $N_{i,p,d}$ is the predicted nuclide concentration, $N_{i,m,d}$ is the measured nuclide concentration, and
309 $\sigma_{i,m,d}$ is the 1σ measurement uncertainty. An error-weighted sum of squares close to two indicates
310 that the difference between the modeled and measured concentrations can be explained by the
311 measurement uncertainty. We consider model runs with an error-weighted sum of squares less
312 than 2.5 to be acceptable fits.

313 We created 2.7-Myr exposure histories using $\delta^{18}\text{O}$ threshold values ranging from 3.60 to
314 4.00‰ (corresponding to 0.7–1.9 Myr cumulative exposure and 0.8–2 Myr cumulative burial over
315 the last 2.7 Myr) at 0.02‰ spacing. For each exposure history, we ran the forward model with
316 subaerial and subglacial erosion rates ranging from 0 to $2.5 \times 10^{-1} \text{ mm yr}^{-1}$ on a log scale (coarse
317 spacing from 0 to $1 \times 10^{-5} \text{ mm yr}^{-1}$ and finer spacing from 1×10^{-5} to $2.5 \times 10^{-1} \text{ mm yr}^{-1}$) to capture
318 the potential range in erosion rates for cold-bedded glaciers and polar environments (e.g., Cook et
319 al., 2020; Koppes et al., 2015; Portenga and Bierman, 2015). Subglacial and subaerial erosion rates
320 are each held constant for all periods of ice cover and exposure, respectively, and therefore we do
321 not consider changes in erosion within glacial cycles or from one glacial cycle to the next. If total
322 (subaerial + subglacial) erosion through a model run is high, a higher proportion of modeled ^{10}Be
323 and ^{26}Al accumulates deep in the rock column where production is low, while less erosion results
324 in a larger fraction of the nuclide production near the surface where production is higher. The two
325 erosion rates may therefore trade-off. For example, an exposure history may yield a good fit to the
326 data with a higher sub-aerial erosion rate and lower sub-glacial erosion rate for a certain sample,
327 as well as with a lower sub-glacial erosion rate and a higher sub-aerial erosion rate. Nevertheless,
328 this model allows us to investigate potential Quaternary erosion and ice cover scenarios across
329 Inglefield Land to test the hypothesis that the variability in our cosmogenic nuclide measurements



330 can be explained with a common 2.7 Myr exposure-burial history and sample-specific subaerial
331 and subglacial erosion rates.

332

333

334

335

336

337

338

339

340

341

342 **4 Results**

343 ***4.1 Mapping***

344 Paleoproterozoic crystalline paragneiss basement rocks are overlain by sub-horizontally bedded
345 Mesoproterozoic to Ordovician sedimentary rocks across Inglefield Land (Fig. 2). Near the ice
346 margin, crystalline basement rocks are exposed, with some areas covered by Quaternary
347 sediments. Along much of the coastline of Inglefield Land, sedimentary rock units extend up to 20
348 km inland, except where erosion incised the cap rock to expose the underlying basement rocks in
349 the four main valleys. North of Hiawatha Glacier, crystalline basement outcrops from the ice
350 margin to the coastline. In total, 48.2% of the surface of Inglefield Land is crystalline basement,
351 29.4% is sedimentary cap rocks, and 17.4% is Quaternary sediments, with the remaining 5% made
352 up of various minor rock units and lakes.



353 The low-elevation coastal (~100 m asl) sites exhibit ice-sculpted bedrock with primary
354 glacial erosional features, including striations (Fig. 3). Smoothed bedrock is also present at the
355 higher-elevation coastal site (255 m asl), though it lacked primary glacial erosional features.
356 Inland, highly weathered bedrock outcrops, often with abundant gruss, rose only a few meters
357 above the surrounding landscape, which is covered by Quaternary sediments composed of
358 weathered, angular boulders. Near the ice margin sites, we also found highly weathered bedrock
359 outcrops exhibiting lots of gruss and weathering pits on rock surfaces.

360 Exposed bedrock fractures are sparse across Inglefield Land, except for the areas west and
361 north of Hiawatha glacier where bedrock fractures are clearly visible at the kilometer-scale (Fig.
362 4). There are sizable fracture zones along Rensselaer Valley and both Marshall valleys; in
363 particular, the fracture zone of the western Marshall Valley extends ~25 km inland. Finally, there
364 are some limited fracture areas in the central inland sector towards the ice sheet.

365 Lakes are abundant across much of Inglefield Land, covering 161 km², (2% of the surface
366 area), but are concentrated in certain sectors (Fig. 5). Regions to the west and north of Hiawatha
367 Glacier have the highest lake densities, with some 1 km² cells 87% covered by lakes. There are
368 also areas of high lake densities towards the coast, particularly near the coastal valleys. Inland, the
369 highest density of lakes is found in central Inglefield Land. Many grid cells do not contain lakes
370 (grid cells not filled in on Fig. 5), or host very small lakes (<1% of grid cell is lake-covered).

371 Taken together, there are clear areas of overlap between exposed crystalline basement rock,
372 bedrock fractures, and high lake densities north of Hiawatha Glacier and in the valleys draining
373 into Rensselaer and Marshall bays (Fig. 6). West of Hiawatha Glacier and in western Inglefield
374 Land, there are large areas of exposed basement rocks with lakes, but no large-scale fractures.



375 There are also a few areas of sedimentary cap rock with high lake densities, most notably between
376 Rensselaer, Marshall, and Dallas bays.

377

378 *4.2 Cosmogenic nuclide analysis*

379 Apparent ^{10}Be ages are generally youngest at our coastal sites and oldest at inland sites. ^{10}Be
380 concentrations are lowest at our ~100 m asl coastal sites, corresponding to apparent exposure ages
381 between 24.9 ± 0.5 and 36.5 ± 1.7 ka (Figs. 6 & 7; Table S1). These sites exhibit ice-sculpting,
382 suggesting short-lived wet-based ice. At the higher elevation coastal site on the western transect
383 (255 m asl), the apparent ^{10}Be age is slightly older – 62.2 ± 1.7 ka. Our oldest apparent exposure
384 ages come from the inland sites on both transects, dating from 99.1 ± 2.4 ka to 213.7 ± 3.5 ka on
385 the western and 87.9 ± 3.8 ka to 215.8 ± 7.4 ka on the eastern transects. We do not observe any
386 relationship between the apparent ^{10}Be exposure age of our inland sites and their elevation or
387 distance along the transect. Ages from the ice margin sites generally fall between those from the
388 coast and inland sites. Apparent ^{10}Be exposure ages from the western ice margin site range from
389 50.2 ± 0.9 ka to 133.7 ± 2.6 ka. At the eastern ice margin site, ^{10}Be ages are between 49.2 ± 0.9 ka
390 and 62.6 ± 1.2 ka.

391 $^{26}\text{Al}/^{10}\text{Be}$ ratios follow a general inverse pattern to the apparent ^{10}Be ages, with the highest
392 ratios (closest to the production ratio) at the coast, lowest ratios inland, and ratios from the ice
393 margin in the middle. At the coastal sites, the three samples taken from ~100 m asl have ratios of
394 6.38 ± 0.44 , 7.58 ± 0.42 , 8.41 ± 0.81 and overlap with the constant exposure isochron with 95%
395 confidence (Fig. 8). The 255 m asl coastal site has a ratio of 5.68 ± 0.30 requiring a minimum
396 burial duration of 500 kyr and at least 25–100 kyr of exposure. In contrast, $^{26}\text{Al}/^{10}\text{Be}$ ratios at our
397 inland sites range from 2.19 ± 0.16 to 5.28 ± 0.30 , with the majority falling between the 500 and



398 1500 kyr burial isochrones and between the 100 and 500 kyr exposure isochrones for total
399 minimum exposure and burial durations of between ~600 and ~2000 kyr. There is one apparent
400 outlier below the 2000 kyr burial isochron with a ratio of 2.19 ± 0.16 (22GRO-03). At the western
401 ice margin site, $^{26}\text{Al}/^{10}\text{Be}$ ratios in our three samples range between 4.00 ± 0.18 and 5.14 ± 0.21 ,
402 corresponding to a minimum glacial history with ~100 and ~250 kyr of cumulative exposure and
403 ~250 – ~1250 kyr of cumulative burial. The boulder has a $^{26}\text{Al}/^{10}\text{Be}$ ratio of 5.15 ± 0.21 , which is
404 the highest ratio at the western ice margin site. At the eastern ice margin site, $^{26}\text{Al}/^{10}\text{Be}$ ratios are
405 between 5.11 ± 0.21 and 5.53 ± 0.26 and represent minimum glacial histories with cumulative
406 exposure durations of ~50–125 kyr and cumulative burial durations of ~500–750 kyr. From both
407 transects, $^{26}\text{Al}/^{10}\text{Be}$ ratios from samples at the ice margin (5.14 ± 0.26 ; mean $\pm 1\sigma$) are slightly
408 higher than those from the inland sites (4.47 ± 0.86 ; excluding the apparent outlier of 2.19 ± 0.16 ;
409 22GRO-03), though these overlap at 1σ uncertainty.

410

411 ***4.3 Constraints on Quaternary ice cover history and erosion***

412 We modeled cosmogenic-nuclide accumulation through the Quaternary to determine whether the
413 measured ^{10}Be and ^{26}Al concentrations across Inglefield Land can be explained by a common
414 exposure history and differential erosion. We tested exposure histories derived from $\delta^{18}\text{O}$
415 thresholds between 3.6 and 4.0‰, corresponding to 0.7–1.9 Myr of cumulative exposure and 0.8–
416 2 Myr of cumulative burial over the last 2.7 Myr. For each of these exposure histories, modeled
417 nuclide concentrations yielded a good fit to those we measured for at least one sample. Yet only
418 the exposure history constructed with a $\delta^{18}\text{O}$ threshold value of 3.74‰ yields ^{10}Be and ^{26}Al
419 concentrations with a good fit to the data in all bedrock samples except those with $^{26}\text{Al}/^{10}\text{Be}$ ratios
420 above the production ratio (22GRO-01 and 22GRD-CR04-SURF) and the sample previously



421 identified as an outlier based on its low $^{26}\text{Al}/^{10}\text{Be}$ ratio (22GRO-03). This best-fitting exposure
422 history corresponds to ~ 0.9 Myr of total exposure and ~ 1.8 Myr of total burial over the last 2.7
423 Myr (Fig. 10). Given this ice-cover scenario, we find model-data agreement with subglacial and
424 subaerial erosion rates ranging between 0 and $\sim 2 \times 10^{-3}$ mm yr $^{-1}$ and 0 and $\sim 2 \times 10^{-2}$ mm yr $^{-1}$,
425 respectively. While there were some exposure and erosion combinations that were compatible with
426 measurements from our single boulder sample (22GRO-32), we prioritized bedrock samples in
427 assessing whether all sites could have a common Quaternary ice-cover history, as the boulder
428 likely has a different exposure history than the collocated bedrock.

429

430

431

432

433

434 **5 Discussion**

435 ***5.1 Differential erosion, ice streams, and ancient landscapes across Inglefield Land***

436 We identified an ancient landscape with our oldest sites retaining at least a ~ 1.5 Myr history.
437 However, the nuclide concentrations vary throughout the landscape despite the fact that the long-
438 term ice-margin history should be similar across sites, as evidenced by recent retreat and advance.
439 After the LGM, the ice sheet retreated over Inglefield Land from its maximum extent in Kane
440 Basin following saddle collapse over Nares Strait. The modern coast deglaciated ~ 8.5 ka, and ice
441 retreated behind the present margin by 6.7 ka (Søndergaard et al., 2020) corresponding to our entire
442 < 50 km transects becoming ice free within 2 kyr. Advance across Inglefield Land was likely
443 similarly swift – for example, Bennike (2002) suggested that the Petermann Glacier advanced at



444 least 25 km in 0.3 kyr towards its Little Ice Age maximum following a mid-Holocene minimum.
445 These findings suggest that – within error of our $^{26}\text{Al}/^{10}\text{Be}$ -derived exposure scenarios – all our
446 sites have experienced similar periods of ice cover and ice-free conditions on glacial-interglacial
447 timescales. This thus begs the question: why do amounts of nuclide inheritance and $^{26}\text{Al}/^{10}\text{Be}$ ratios
448 at our coastal, inland, and ice-margin sites differ?

449 Our combined mapping of bedrock lithology, landscape-scale fractures, and lake density
450 as evidence for past glacial erosion, along with field observations of bedrock surface weathering
451 provide a first hint that erosion is responsible for differing ^{26}Al and ^{10}Be concentrations. Though
452 some of the cap rock removal likely occurred before the Quaternary (e.g., Krabbendam and
453 Bradwell, 2014), our other mapping reveals a clear imprint of differential erosion by the ice sheet.
454 Regions of crystalline bedrock and high lake density inland (with the exception of the areas
455 fronting Hiawatha Glacier) and near the ice margin exhibit weathered bedrock surfaces, diagnostic
456 of cold-based ice cover during the last glacial cycle. Overlapping areas of crystalline bedrock,
457 fractures, and high lake densities in the four valleys leading into Force, Rensselaer, and Dallas
458 bays and in front of Hiawatha Glacier, however, contain fresh, unweathered bedrock outcrops with
459 primary surface features intact. The prevalence of erosion indicators in these areas suggests a role
460 for erosive ice with higher velocities than experienced by the surrounding landscape for at least a
461 portion of the last glacial cycle. We posit that these areas were ice stream onset zones during the
462 last glacial cycle and likely earlier glacial cycles as well.

463 The $^{26}\text{Al}/^{10}\text{Be}$ ratios and lower levels of cosmogenic nuclide inheritance support more
464 erosion at the coastal sites versus the inland and ice margin areas. The samples at 100 m asl in
465 Rensselaer and Marshall valleys have the youngest apparent exposure ages and $^{26}\text{Al}/^{10}\text{Be}$ ratios
466 close to the production ratio, suggesting removal of the longer burial signal preserved at the upland



467 sites via erosion. Furthermore, the 255 m asl coastal site in Rensselaer Valley has more inheritance
468 and lower $^{26}\text{Al}/^{10}\text{Be}$ ratios compared to the 100 m asl elevation site, which may reflect differential
469 erosion by an ice stream in the Rensselaer Valley as it increased velocity and erosion down flow.
470 Previous studies on Baffin Island and in Scandinavia used mapping and cosmogenic nuclide
471 measurements to identify areas as ice stream onset zones (Andersen et al., 2018; Briner et al., 2006;
472 Briner et al., 2008; Brook et al., 1996). Ice at these onset zones transitioned from cold-based to
473 warm-based ice and did not erode >3 m during the last glacial cycle, though it is thought that
474 velocities increased downstream from these areas. We find similar cosmogenic nuclide evidence
475 of ice stream onset zones at the mouths of Rensselaer and Marshall bays, suggesting that ice
476 streams may have initiated in these areas during glacial maxima.

477 Cosmogenic nuclide concentrations in weathered bedrock surfaces at our inland and ice
478 margin sites retain combined minimum exposure and burial signals of 500 kyr to 1500 kyr,
479 demonstrating the antiquity of Inglefield Land. The preservation of these inland and ice margin
480 landscapes implies past cold-based ice conditions and, in turn, low erosion across Inglefield Land
481 through multiple glacial cycles. This also suggests the erosional landscapes seen in mapping across
482 the interior of Inglefield Land (i.e., lack of cap rocks and exposed crystalline basement, high lake
483 densities, and bedrock fractures) were created prior to the last glaciation.

484 Such old, low-erosion landscapes have been preserved in other glaciated parts of the Arctic.
485 Our results are similar to studies from southern, western, northwestern, and northeastern Greenland
486 and Baffin Island that identify long-preserved (often > 1000 kyr), ancient landscapes with low
487 amounts of erosion and high amounts of cosmogenic nuclide inheritance (Andersen et al., 2020;
488 Beel et al., 2016; Bierman et al., 1999; Briner et al., 2006; Ceperley et al., 2020; Corbett et al.,
489 2016a; Miller et al., 2006; Roberts et al., 2013; Sbarra et al., 2022; Skov et al., 2020; Søndergaard



490 et al., 2020). Similarly, the pattern of significantly lower cosmogenic nuclide inventories at lower,
491 coastal areas in less preserved landscapes is seen elsewhere in Greenland and the Canadian Arctic.
492 In eastern Greenland, for example, Skov et al. (2020) found higher degrees of cosmogenic nuclide
493 inheritance in weathered bedrock uplands and lower concentrations in sculpted bedrock closer to
494 the coast around Dove Bugt, attributing this to a polythermal ice sheet with efficient erosion at
495 lower elevations. Studies on Baffin Island using ^{10}Be and ^{26}Al measurements found transitions
496 from cold-based and non-erosive to warm-based and erosive ice at lower elevations near the coast
497 (e.g., Briner et al., 2006; Briner et al., 2008), supporting our conclusions of transitions from cold-
498 based to warm-based ice near the coast of Inglefield Land.

499

500

501

502

503 ***5.3 Can measured $^{26}\text{Al}/^{10}\text{Be}$ ratio differences be explained with a common ice-cover history and***
504 ***variable erosion rates?***

505 We tested our hypothesis that the disparate nuclide concentrations across Inglefield Land could
506 have resulted from a shared Quaternary exposure history and differential erosion. Indeed, we found
507 that the ^{10}Be and ^{26}Al concentrations in most of our bedrock samples can be explained through a
508 Pleistocene ice-cover history with 0.9 Myr cumulative exposure and 1.8 Myr cumulative burial,
509 and sample-varying subglacial and subaerial erosion rates.

510 The range of sub-aerial erosion rates (0 mm yr^{-1} and $2 \times 10^{-2} \text{ mm yr}^{-1}$) that provide good
511 fits to the measured nuclide concentrations for our preferred exposure history are broadly
512 consistent with sub-aerial erosion rates measured in other cold, arid, polar environments. A global



513 synthesis found mean subaerial erosion rates at rock outcrops are 13×10^{-3} , 8×10^{-3} , and 4×10^{-3}
514 mm yr^{-1} in cold, arid, and polar environments, respectively (Portenga and Bierman 2011). A
515 cosmogenic nuclide-based study from the southern Ellsworth Mountains, Antarctica found longer-
516 term subaerial erosion rates of $5.52 \times 10^{-3} \pm 0.26 \times 10^{-3} \text{ mm yr}^{-1}$ for gneiss (Marrero et al., 2018),
517 similar to those derived from Baffin Island gneiss of $2 \times 10^{-3} \text{ mm/yr}$ (Margreth et al., 2016).
518 Furthermore, subaerial erosion of gneiss in the polar regions is thought to occur primarily through
519 mineral- and granular-scale processes, including abrasion and disintegration, and are accelerated
520 by wind-blown sediments (Margreth et al., 2016). We noted abundant gruss around our inland and
521 ice-margin sites and near constant winds with wind-transported sediments, suggesting that these
522 processes may be responsible for subaerial erosion in Inglefield Land.

523 Subglacial erosion rates that yield good model-data fits are between 0 and $\sim 2 \times 10^{-2} \text{ mm}$
524 yr^{-1} and are generally lower than those measured elsewhere in Greenland. Many of these previous
525 estimates, however, come from warm-based glaciers, while Inglefield Land was covered primarily
526 by cold-based ice. The upper range of our modeled sub-glacial erosion rates agree with those from
527 east Greenland derived from sediment flux data of $1 - 4 \times 10^{-2} \text{ mm yr}^{-1}$ (Andrews et al., 1994),
528 though this was later updated by Cowton et al. (2012) to $3 \times 10^{-1} \text{ mm yr}^{-1}$ to account for sediment
529 entrained in icebergs (Syvitski et al., 1996). In central-west Greenland, suspended sediment
530 measurements from the Watson River yielded average subglacial erosion rates of $5 \times 10^{-1} \text{ mm}$
531 yr^{-1} , with annual erosion rates as high as 4.5 mm yr^{-1} and $4.8 \pm 2.6 \text{ mm yr}^{-1}$, all higher than our
532 modeled rates (Cowton et al., 2012; Hasholt et al., 2018; Hogan et al., 2020). Glaciomarine
533 deposits near Petermann Glacier, northwest Greenland and at the mouth of Jakobshavn Isfjord
534 constrain erosion rates during the last deglaciation to $0.29 - 0.34 \text{ mm yr}^{-1}$ and 0.52 mm yr^{-1} ,
535 respectively (Hogan et al., 2012; Hogan et al., 2020). Finally, Balter-Kennedy et al. (2021)



536 determined centennial-scale subglacial erosion rates of $3\text{--}8 \times 10^{-1} \text{ mm yr}^{-1}$ and orbital-scale rates
537 of $1\text{--}3 \times 10^{-1} \text{ mm yr}^{-1}$ near Jakobshavn Isbræ. While these previously derived subglacial erosion
538 rates are likely higher than what we report because they come from places with different ice sheet
539 thermal states, these estimates of subglacial erosion reflect periods when temperatures were
540 generally warmer or periods of warming, which can lead to higher subglacial erosion rates because
541 of increased basal temperatures and subglacial sliding (Alley et al., 2019).

542 Cold-bedded glaciers are commonly considered non-erosive, yet glacial erosional features
543 (striae, scrapes, grooves, and isolated blocks) in landscapes otherwise protected by cold-based ice
544 demonstrate their erosional capacity (Atkins et al., 2002; Cuffey et al., 2000; Sugden, 1978;
545 Sugden et al., 2005; Ugelvig and Egholm, 2018). Our modeled sub-glacial erosion rates between
546 0 and $\sim 2 \times 10^{-2} \text{ mm yr}^{-1}$ in mapped areas of cold-based ice cover point to the erosive nature of cold-
547 based glaciers and are consistent with previous estimates of erosion. Syntheses found modern sub-
548 glacial erosion rates under frozen-bedded glaciers on the Antarctic Peninsula to be between 1×10^{-2}
549 2 and $1 \times 10^{-1} \text{ mm yr}^{-1}$, (Koppes et al., 2015), while on the Meserve Glacier, a cold-based alpine
550 glacier in Victoria Land, Antarctica, subglacial erosion rates have been estimated to be 2×10^{-3}
551 mm yr^{-1} (Cuffey et al., 2000). Studies of tors in the Cairngorm Mountains, Scotland, yield
552 subglacial erosion estimates of $\sim 4.4 \times 10^{-3} \text{ mm yr}^{-1}$ during cover by a cold-based Celtic Ice Sheet
553 (Phillips et al., 2006). Various mechanisms have been proposed for erosion by cold-bedded
554 glaciers. Frozen bedded glaciers entrain debris at their bed and can minorly abrade and pluck
555 bedrock surfaces (Atkins et al., 2002; Cuffey et al., 2000; Sugden, 1978; Sugden et al., 2005;
556 Ugelvig and Egholm, 2018). Extensive studies from the Cairngorm Mountains in Scotland using
557 cosmogenic nuclides and geomorphic models of tor formation and erosion found cold-based ice



558 erosion was potentially capable of significantly modifying pre-existing landforms (Goodfellow et
559 al., 2014; Hall and Glasser, 2003; Hall and Phillips, 2006; Phillips et al., 2006).

560 In sum, we find that the disparate nuclide concentrations across Inglefield Land can be
561 explained by a common Quaternary exposure/burial history if differential erosion is invoked.
562 Erosion rates consistent with the cosmogenic data are consistent with others found in polar areas
563 covered by cold-based glaciers. Variability in erosion rates across the landscape likely reflect
564 differences in lithology, as well as subglacial conditions. Spatial variability in erosion is captured
565 in our model, and may be due to local differences in lithology (e.g., mineralogy and crystal size)
566 and landscape position. However, our model does not account for temporal variability in sub-
567 glacial erosion. Temporal variability (abrasion versus quarrying) should be diminished when
568 averaged across many glacial cycles, but the imprint of variable glacial erosion during the last
569 glacial cycle (e.g., a site of cobble-sized block of bedrock removed beneath mostly frozen ice;
570 Atkins et al., 2002; Hall and Phillips, 2006) may lead to differences in the resulting sub-glacial
571 erosion rates. Furthermore, the basal zone across Inglefield Land may have transitioned from less-
572 erosive to more-erosive and back to less-erosive during switches between warm- and cold-bedded
573 conditions through the thickening and thinning of the ice sheet during a glacial cycle. This could
574 lead to time-varying sub-glacial erosion rates and shorter periods of increased glacial erosion, as
575 evidenced by the glacial sculpting at our coastal sites.

576

577 ***5.4 Long-term ice sheet fluctuations across Inglefield Land***

578 $^{26}\text{Al}/^{10}\text{Be}$ ratios from our oldest bedrock surfaces suggest that, at a minimum, the Greenland Ice
579 Sheet covered Inglefield Land for 1200 kyr and was smaller than today for 400 kyr over the last
580 1600 kyr. We determined that a Quaternary exposure history with ~ 0.9 Myr of cumulative



581 exposure and ~1.8 Myr of cumulative burial (constructed using a $\delta^{18}\text{O}$ threshold of 3.74‰) is
582 consistent with the measured cosmogenic-nuclide concentrations in nearly all of our bedrock
583 surfaces when erosion rates are allowed to vary for each sample. In this preferred exposure
584 scenario, much of the exposure takes place between 2.7 and 1.2 Ma before the mid-Pleistocene
585 transition, but still requires ice-free conditions (and exposure) within the last ~1.2 Myr during
586 major interglacials.. These periods of exposure are of particular interest as they indicate times
587 when the Greenland Ice Sheet was at its present extent or smaller.

588 Our results complement limited other terrestrial studies of Greenland Ice Sheet stability
589 throughout the Quaternary. $^{26}\text{Al}/^{10}\text{Be}$ measurements from the GISP2 bedrock core from under the
590 center of the Greenland Ice Sheet revealed that the ice sheet was present for most of the Quaternary
591 but was nearly completely absent at least once in the last 1.1 Myr (Schaefer et al., 2016). Studies
592 of basal material from Camp Century show similar results, supporting that the northwestern
593 Greenland Ice Sheet was present through most of the Pleistocene (Christ et al., 2021). Additionally,
594 when compared to studies these of material from under the modern Greenland Ice Sheet, our results
595 suggest that Inglefield Land was ice-free throughout much more of the Quaternary than interior
596 sectors (i.e., currently covered by the modern ice sheet), logical given that Inglefield Land would
597 be completely covered only during glacial maxima. When taken at face-value, our preferred
598 exposure history corresponding to a $\delta^{18}\text{O}$ threshold of 3.74‰ indicates that the northwestern
599 Greenland Ice Sheet persisted at an extent larger-than-today throughout some Pleistocene
600 interglacials, further supported by similar findings from the Laurentide Ice Sheet (Leblanc et al.,
601 2023).

602

603



604 **6 Conclusions**

- 605 • Geologic mapping partitions Inglefield Land into zones of glacial erosion and protection
606 revealing restricted zones of erosion in lower Force, Rensselaer, and Marshall valleys and
607 in front of Hiawatha Glacier as ice-velocity increased coastward into ice streams;
608 elsewhere landscapes were likely covered by low erosion (e.g., frozen-bedded) regimes.
- 609 • Patterns of glacial erosion are confirmed with cosmogenic nuclide measurements,
610 revealing an ancient landscape. This implies widespread cold-based ice cover across much
611 of Inglefield Land during Quaternary glacial cycles, even during transitions between
612 interglacial and glacial periods. These measurements also indicate that, despite cosmogenic
613 nuclide inheritance, there was perhaps temporarily warm-based ice at coastal sites during
614 the last glacial cycle when the Greenland Ice Sheet extended well beyond Inglefield Land,
615 and ice streams originated near the mouths of the modern Force, Rensselaer, and Marshall
616 bays. Mapping and cosmogenic nuclide measurements allow us to differentiate between
617 areas of cold- and warm-based ice offering a clear look into the polythermal nature of
618 former ice sheets.
- 619 • Differential subglacial and subaerial erosion explains disparate cosmogenic nuclide
620 concentrations found at our inland and ice margin sites. Modeled subaerial erosion rates
621 match those found in other polar regions for similar lithologies. Our modeled subglacial
622 erosion rates are lower than those previously calculated for Greenland, as other studies
623 focused on warm-based parts of the Greenland Ice Sheet. We provide estimates of
624 subglacial erosion under cold-bedded conditions.
- 625 • Ice cover durations derived from $^{26}\text{Al}/^{10}\text{Be}$ ratios and cosmogenic nuclide modeling reveal
626 a common ice sheet history, and variable erosion rates indicate that the ice sheet



627 persistently covered Inglefield Land for approximately one-third of the last 2.7 Myr. This
628 exposure occurred mostly early in the Quaternary before the mid-Pleistocene transition.
629 Like other findings (e.g., LeBlanc et al., 2023), when taken at face value, our $\delta^{18}\text{O}$ threshold
630 value when applied to the global $\delta^{18}\text{O}$ stack implies ice-cover during some middle and late
631 Pleistocene interglacials. Our results also suggest that the Greenland Ice Sheet was at its
632 current extent or smaller during several interglacial periods, adding to the body of literature
633 that indicate a dynamic Greenland Ice Sheet throughout the Quaternary.

634 • Bedrock surfaces across much of Inglefield Land were not greatly eroded during the LGM
635 and contain a long-term cosmogenic nuclide memory of ice sheet fluctuations through the
636 mid-Pleistocene – at a minimum. Our bedrock sampling strategy and measurements
637 provide an analog for information contained in sub-ice material under the Greenland Ice
638 Sheet, indicating that this material should contain valuable cosmogenic nuclide archives of
639 ice sheet change during minimum phases.

640

641

642 **Code availability**

643 All MATLAB codes and data used in the study are provided in the supplementary materials.

644

645 **Data availability**

646 All cosmogenic nuclide data required to calculate exposure ages are included in the supplementary
647 materials.

648

649



650 **Financial support**

651 CKW and JPB were supported by NSF grant #1933938 and ABK, JMS, and NEY were supported
652 by NSF grant #1933927.

653

654 **Author contributions**

655 All authors designed the study and conducted fieldwork. CKW undertook GIS mapping and lab
656 work. ABK led modeling of cosmogenic nuclide results. CKW, JPB, and ABK wrote the first draft
657 of the manuscript and created all figures. All authors edited and contributed to subsequent
658 manuscript drafts.

659

660 **Competing interests**

661 The authors declare that they have no conflict of interest.

662 **Acknowledgements**

663 Inglefield Land is part of the lands traditionally inhabited by the Inughuit. We thank the people
664 and government of Greenland for allowing us to conduct fieldwork on the island, service people
665 and workers at Pittufik Space Base for their hospitality, Kyli Cosper at Polar Field Services for
666 logistical support, Air Greenland for helicopter flights, Karlee Prince, Red Stein, Brandon Graham,
667 and Jen Smola for help in the field, and Roseanne Schwartz and Maya Lasker for lab assistance.

668

669

670

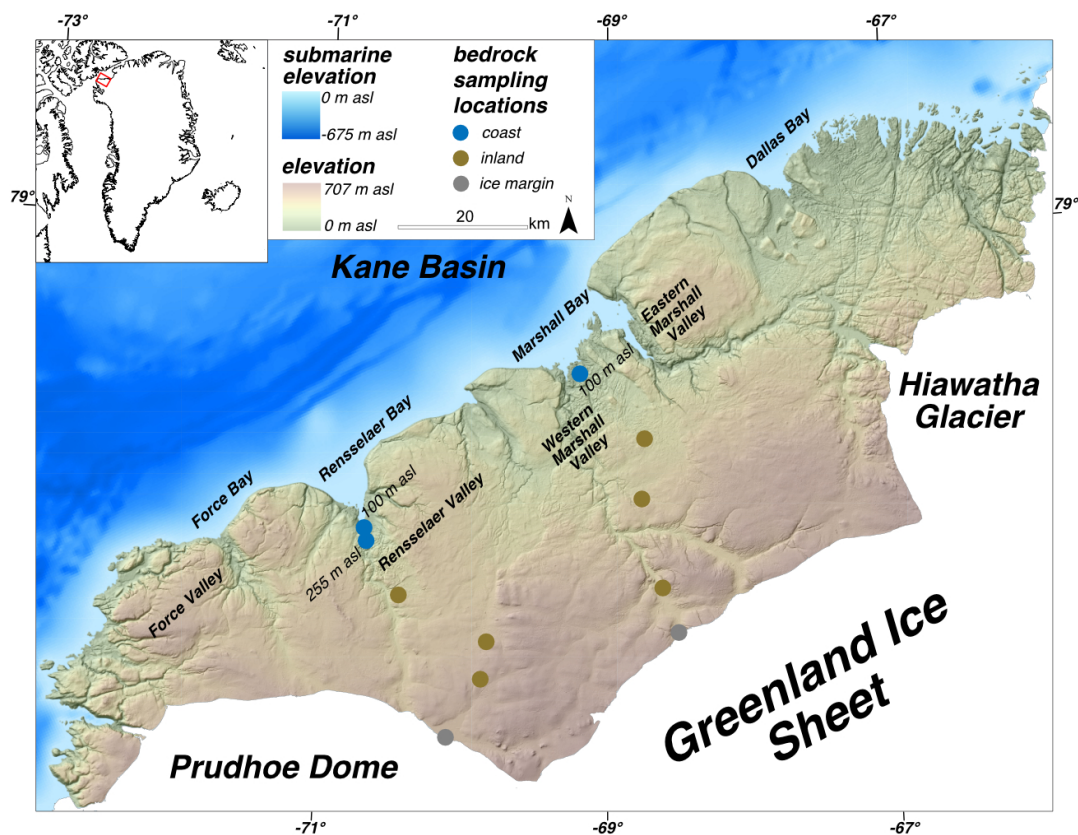
671

672



673 **Figures**

674



675

676 *Figure 1: Overview map of Ingfield Land and key geographic locations.*

677

678

679

680

681

682

683

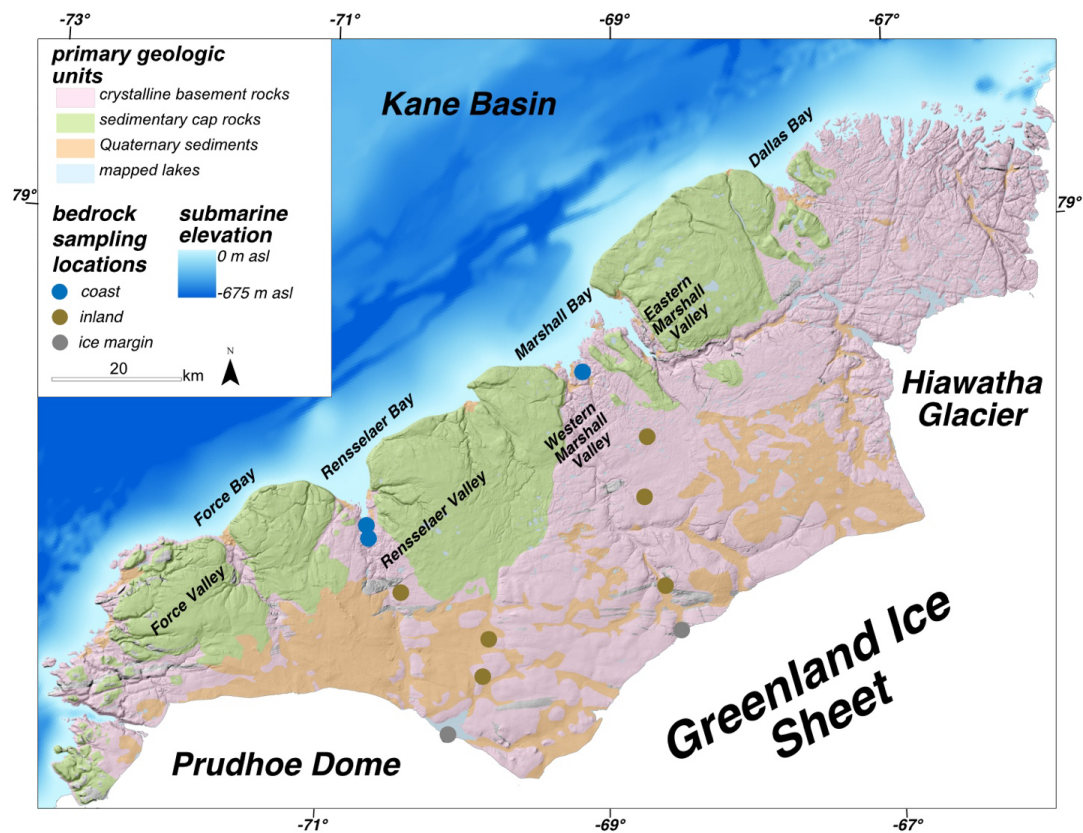
684

685



686

687



688

689 *Figure 2: simplified geologic map of Inglefield Land.*

690

691

692

693

694

695

696

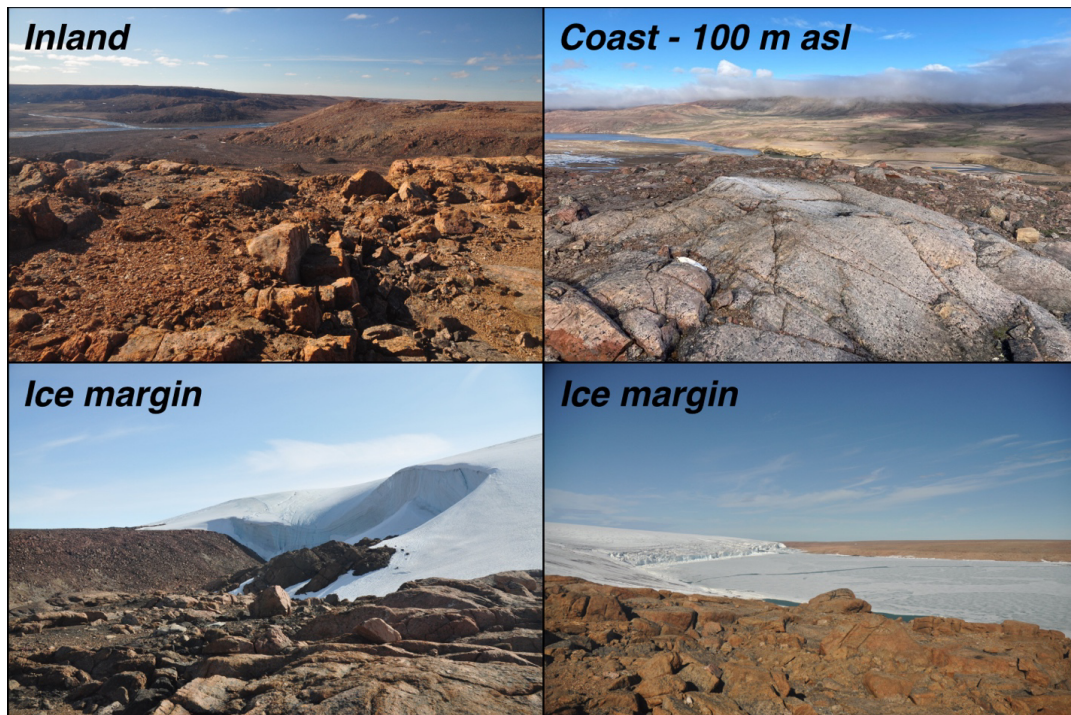
697

698

699



700



701

702

703 *Figure 3: representative images of bedrock surfaces at sample sites in Inglefield Land.*

704

705

706

707

708

709

710

711

712

713

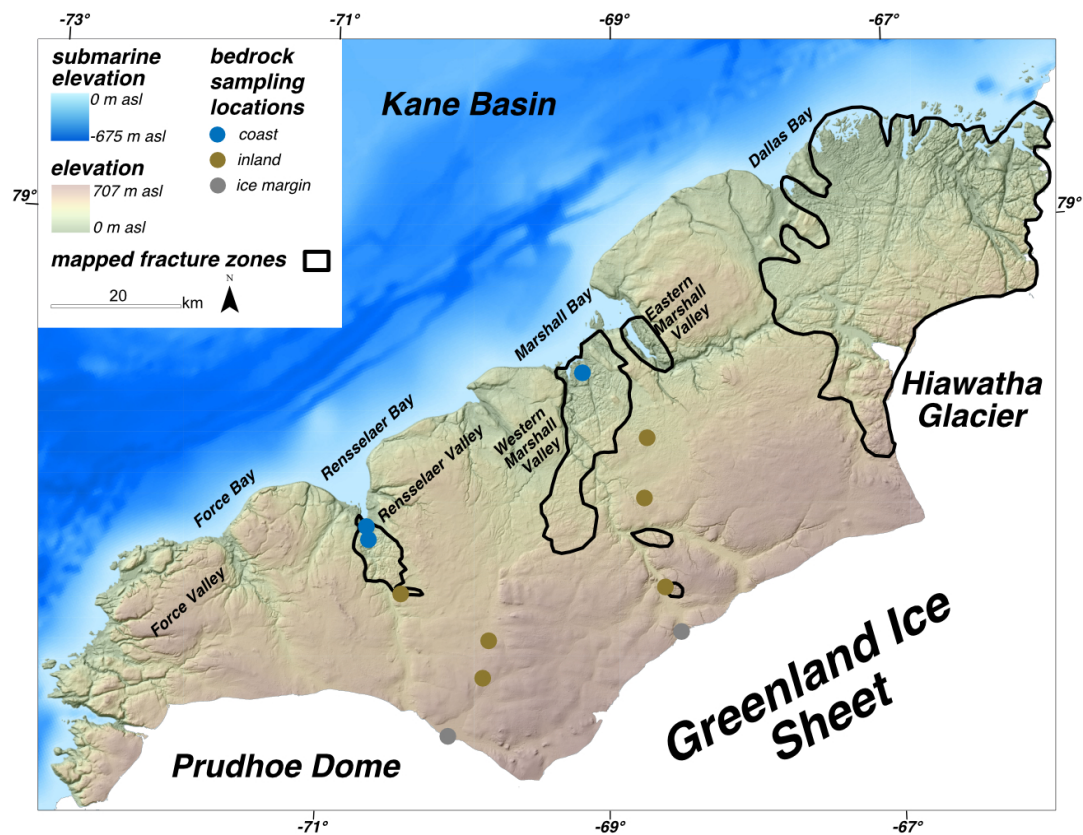
714

715



716

717



718

719 *Figure 4: mapped fracture zones in Inglefield Land.*

720

721

722

723

724

725

726

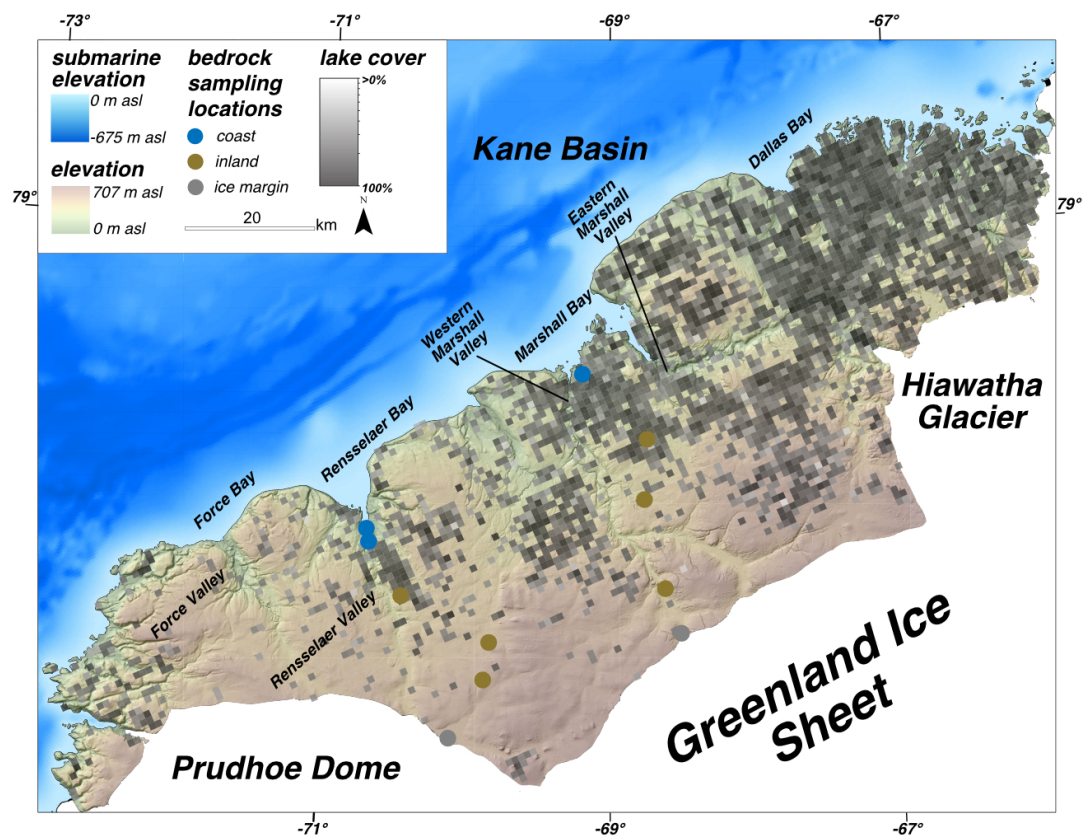
727

728

729



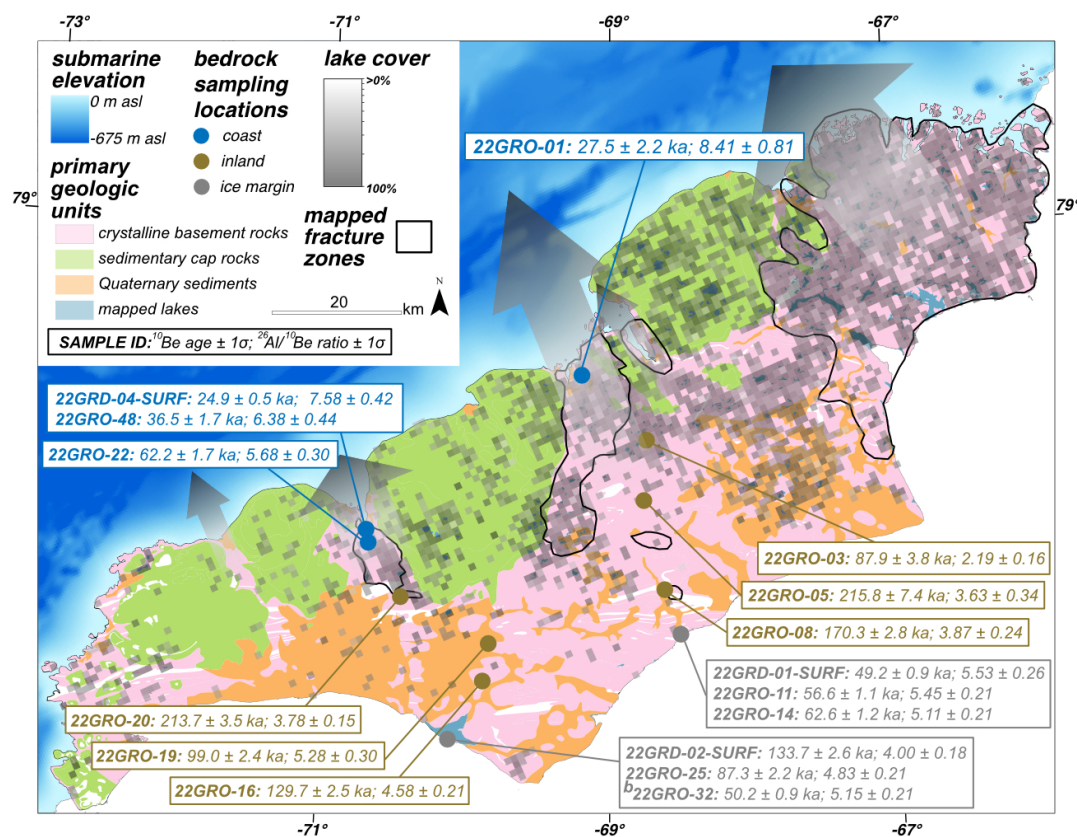
730
731
732
733
734
735
736



737
738
739
740
741
742
743

Figure 5: map of lake densities across Ingfield Land. Grid cells are 1 km².

744
 745
 746
 747
 748
 749
 750
 751



752
 753
 754
 755
 756
 757

Figure 6: combined map of bedrock lithology, fracture zones, and lake densities with cosmogenic nuclide results. Semi-transparent arrows show zones of increasing erosion as indicated by mapping proxies.



758

759 *Figure 7: subset of bedrock sample photos and resultant cosmogenic nuclide results.*

760

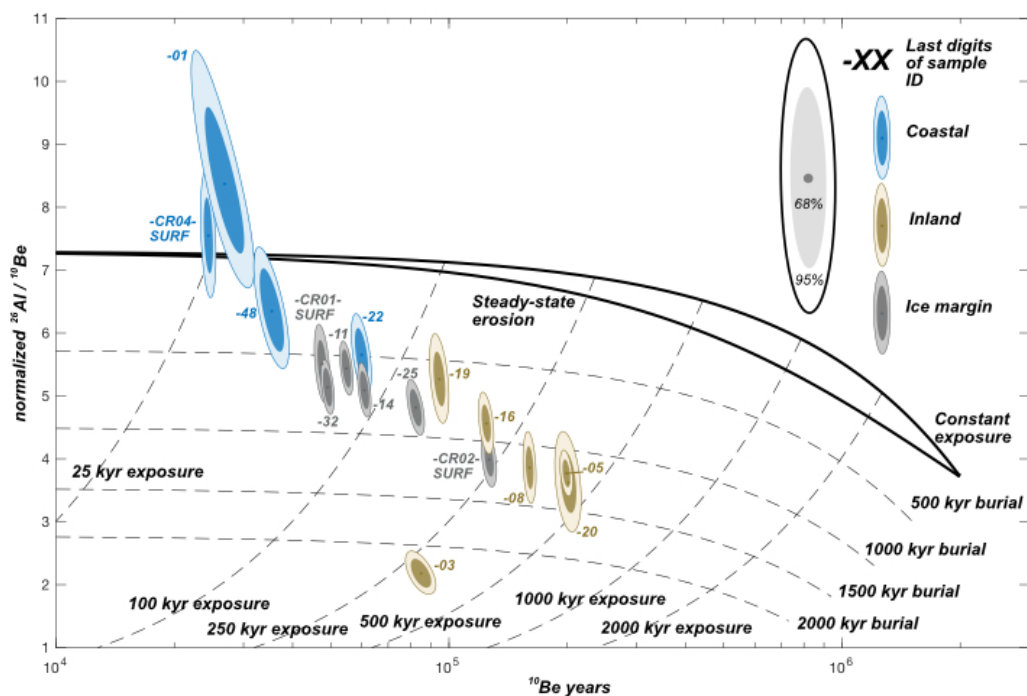
761

762

763



764
765
766
767
768
769
770

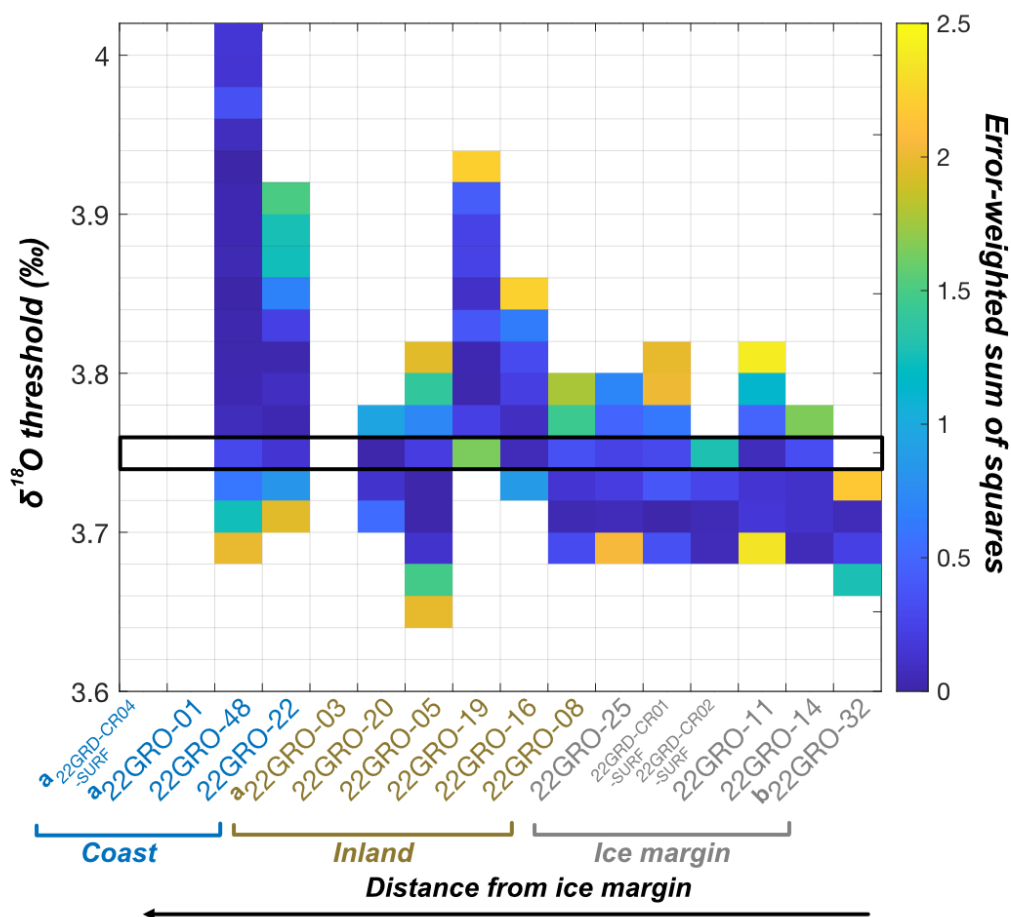


771
772
773
774
775
776
777
778
779
780

Figure 8: $^{26}\text{Al}/^{10}\text{Be}$ two-nuclide diagram. Concentrations normalized to Arctic high latitude, sea level ^{10}Be production rate of $3.96 \text{ atoms g yr}^{-1}$ using Greenland-specific $^{26}\text{Al}/^{10}\text{Be}$ surface production ratio of 7.3 (Corbett et al., 2016; Young et al., 2013).



781
 782
 783



784

785 *Figure 9: Model-data fits for exposure histories constructed with $\delta^{18}O$ thresholds of 3.60-4.00‰. For each $\delta^{18}O$*
 786 *threshold, we modeled cosmogenic nuclide concentrations for each sample using subaerial and subglacial erosion*
 787 *rates ranging from 0 to $2.5 \times 10^{-1} \text{ mm yr}^{-1} \text{ mm/yr}$. Colored tiles show the best/lowest error-weighted sums of squares*
 788 *(EWSS) for each sample and $\delta^{18}O$ threshold across all tested erosion rate combinations. We consider an EWSS <2.5*
 789 *to be an acceptable model-data fit. White tiles indicate that no combination of erosion rates yielded an EWSS <2.5.*
 790 *An exposure history constructed with a $\delta^{18}O$ threshold of 3.74‰, outlined in black box, was the only exposure history*
 791 *we tested that gave an acceptable fit for all non-outlier bedrock samples. ^aoutlier samples identified with $^{26}Al/^{10}Be$*
 792 *ratios. ^bboulder sample.*

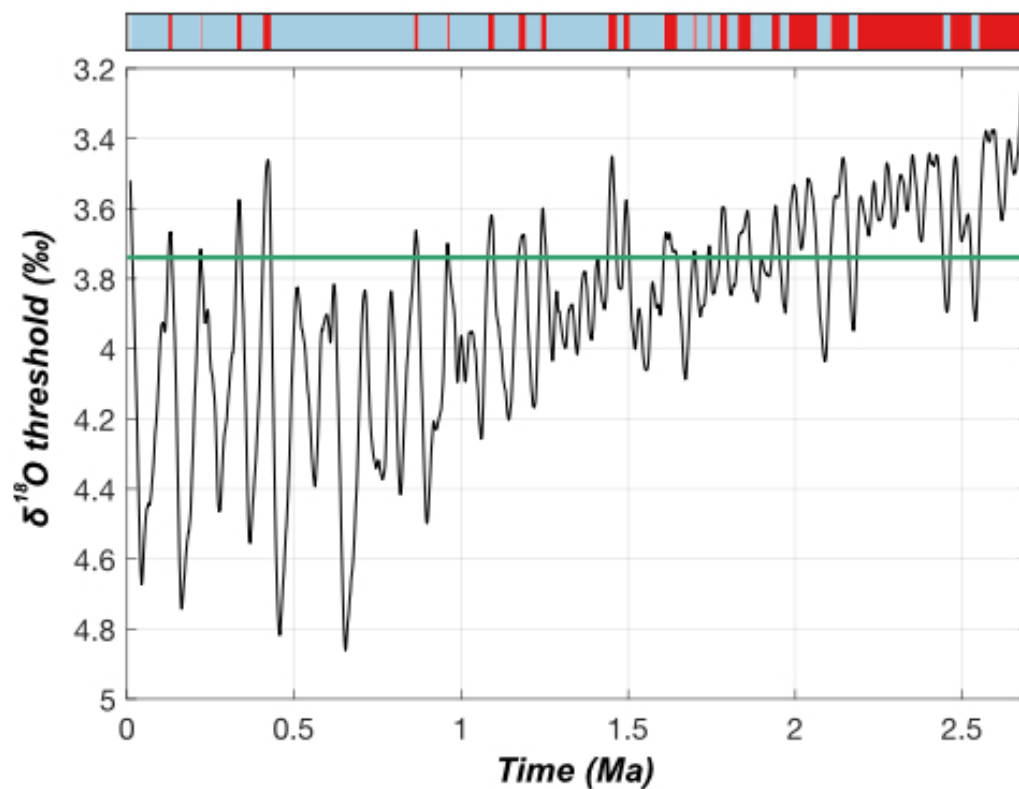
793

794



795

796



797

798

799 *Figure 10: Exposure history constructed with a 3.74‰ $\delta^{18}\text{O}$ threshold (teal line) on the LR04 stack (Lisiecki and*
800 *Raymo, 2005), below which we considered the site ice-free and above which we considered the site ice-covered. The*
801 *resulting exposure history is shown in the top panel, where periods of exposure are red, and periods of burial are*
802 *blue. This is the only exposure history we tested that, even when considering site-specific subaerial and subglacial*
803 *erosion rates, yielded an acceptable fit for all non-outlier bedrock samples.*

804

805

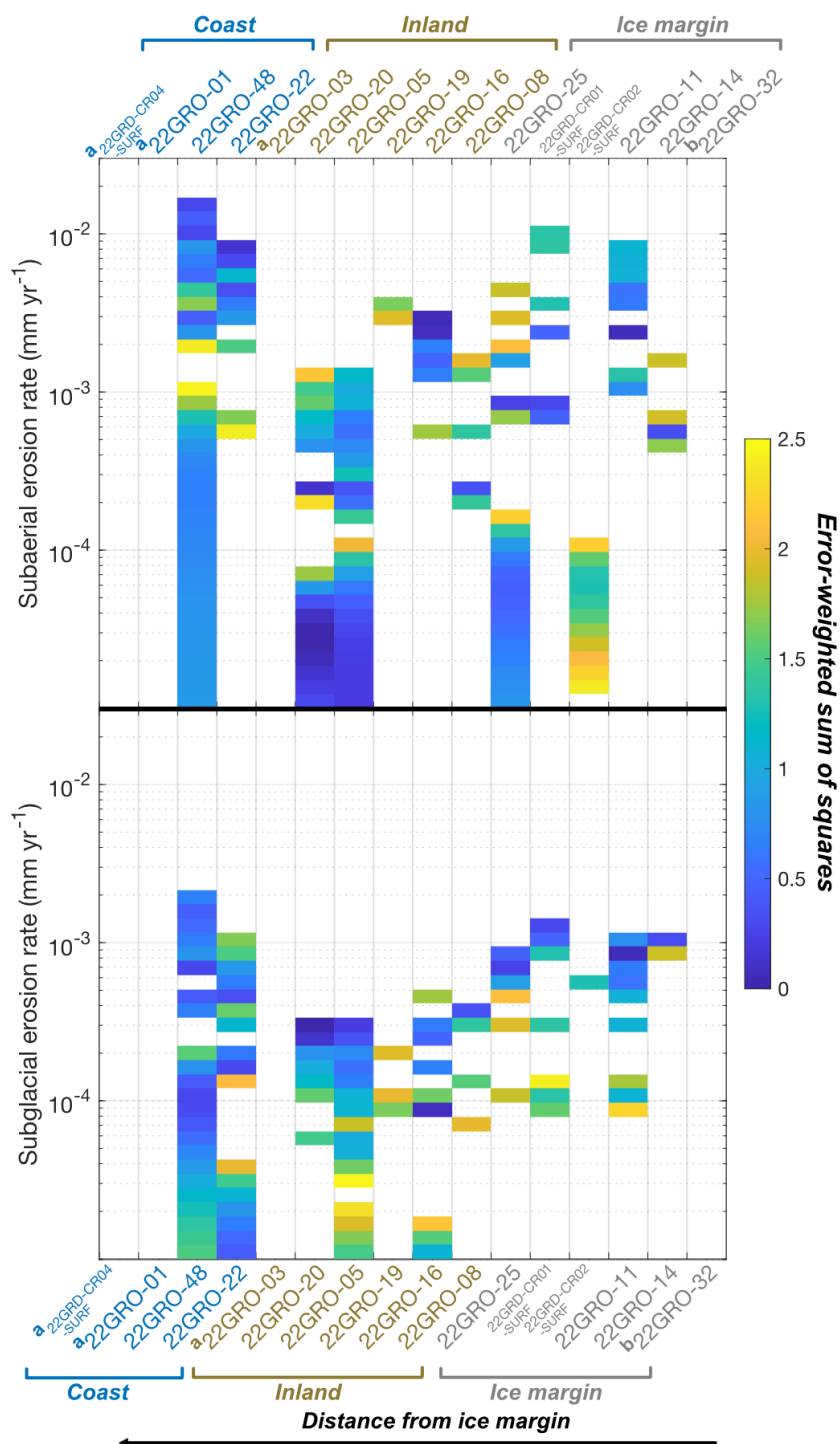
806

807

808

809

810





812 *Figure 11: Model-data fits for tested subaerial (top) and subglacial (bottom) erosion rates for our preferred exposure*
813 *history constructed with a $\delta^{18}O$ threshold of 3.74‰. Colored tiles show the best/lowest error-weighted sums of squares*
814 *for tested erosion rate for each sample. White tiles indicate that, for this exposure history, there is no combination of*
815 *subaerial and subglacial erosion that yield a good fit to the data. For example, in combination with subaerial erosion,*
816 *only one tested subglacial erosion rate ($5 \times 10^{-4} \text{ mm yr}^{-1}$) yielded an acceptable fit for sample 22GRD-CR02-SURF.*
817 *Yet, when applying that subglacial erosion rate, subaerial erosion rates ranging from $0.2\text{--}1.2 \times 10^{-4} \text{ mm yr}^{-1}$ yielded*
818 *an acceptable model-data fit. We tested subaerial and subglacial erosion rates from 0 to $2.5 \times 10^{-1} \text{ mm yr}^{-1}$. For no*
819 *sample was there an acceptable model-data fit for the preferred exposure history when either erosion rate was >2.5*
820 *$\times 10^{-2} \text{ mm yr}^{-1}$. In addition, any sample that yielded a good model-data fit for an erosion rate of $1 \times 10^{-5} \text{ mm yr}^{-1}$, we*
821 *also found good fits down to 0 mm yr^{-1} (no erosion of that type). For clarity, the y-axis for both panels is restricted to*
822 *1×10^{-5} to $2.5 \times 10^{-2} \text{ mm yr}^{-1}$. ^aoutliers identified from $^{26}\text{Al}/^{10}\text{Be}$ ratios. ^bboulder sample.*

823

824

825

826

827

828

829

830

831

832

833

834

835

836

837

838

839

840

841



842 References

- 843 Alley, R. B., Cuffey, K. M., and Zoet, L. K.: Glacial erosion: status and outlook, *Annals of*
844 *Glaciology*, 60, 1-13, 10.1017/aog.2019.38, 2019.
- 845 Andersen, J. L., Egholm, D. L., Olsen, J., Larsen, N. K., and Knudsen, M. F.: Topographical
846 evolution and glaciation history of South Greenland constrained by paired 26Al/10Be
847 nuclides, *Earth and Planetary Science Letters*, 542, 116300,
848 <https://doi.org/10.1016/j.epsl.2020.116300>, 2020.
- 849 Andersen, J. L., Egholm, D. L., Knudsen, M. F., Linge, H., Jansen, J. D., Pedersen, V. K., Nielsen,
850 S. B., Tikhomirov, D., Olsen, J., and Fabel, D.: Widespread erosion on high plateaus during
851 recent glaciations in Scandinavia, *Nature Communications*, 9, 830,
852 <https://doi.org/10.1038/s41467-018-03280-2>, 2018.
- 853 Andrews, J. T., Clark, P. U., and Stravers, J. A.: The patterns of glacial erosion across the eastern
854 Canadian Arctic, Quaternary environments: Eastern Canadian Arctic, Baffin Bay, and
855 West Greenland. Edited by JT Andrews. Allen and Unwin, Winchester, Massachusetts, 69-
856 92, 1985.
- 857 Andrews, J. T., Milliman, J. D., Jennings, A. E., Rynes, N., and Dwyer, J.: Sediment Thicknesses
858 and Holocene Glacial Marine Sedimentation Rates in Three East Greenland Fjords (ca.
859 68°N), *The Journal of Geology*, 102, 669-683, 10.1086/629711, 1994.
- 860 Aschwanden, A. and Brinkerhoff, D. J.: Calibrated mass loss predictions for the Greenland Ice
861 Sheet, *Geophysical Research Letters*, n/a, e2022GL099058,
862 <https://doi.org/10.1029/2022GL099058>, 2022.
- 863 Atkins, C. B., Barrett, P. J., and Hicock, S. R.: Cold glaciers erode and deposit: Evidence from
864 Allan Hills, Antarctica, *Geology*, 30, 659-662, 10.1130/0091-
865 7613(2002)030<0659:CGEAD>2.0.CO;2, 2002.
- 866 Balco, G.: Production rate calculations for cosmic-ray-muon-produced 10Be and 26Al
867 benchmarked against geological calibration data, *Quaternary Geochronology*, 39, 150-173,
868 <https://doi.org/10.1016/j.quageo.2017.02.001>, 2017.
- 869 Balco, G., Stone, J. O., Lifton, N. A., and Dunai, T. J.: A complete and easily accessible means of
870 calculating surface exposure ages or erosion rates from 10Be and 26Al measurements,
871 *Quaternary Geochronology*, 3, 174-195, <https://doi.org/10.1016/j.quageo.2007.12.001>,
872 2008.
- 873 Balco, G., Brown, N., Nichols, K., Venturelli, R. A., Adams, J., Braddock, S., Campbell, S.,
874 Goehring, B., Johnson, J. S., and Rood, D. H.: Reversible ice sheet thinning in the
875 Amundsen Sea Embayment during the Late Holocene, *The Cryosphere*, 17, 1787-1801,
876 <https://doi.org/10.5194/tc-17-1787-2023>, 2023.
- 877 Balter-Kennedy, A., Young, N. E., Briner, J. P., Graham, B. L., and Schaefer, J. M.: Centennial-
878 and Orbital-Scale Erosion Beneath the Greenland Ice Sheet Near Jakobshavn Isbræ,
879 *Journal of Geophysical Research: Earth Surface*, 126, e2021JF006429,
880 <https://doi.org/10.1029/2021JF006429>, 2021.
- 881 Batchelor, C. L., Krawczyk, D. W., O'Brien, E., and Mulder, J.: Shelf-break glaciation and an
882 extensive ice shelf beyond northwest Greenland at the Last Glacial Maximum, *Marine*
883 *Geology*, 476, 107375, <https://doi.org/10.1016/j.margeo.2024.107375>, 2024.
- 884 Beel, C. R., Lifton, N. A., Briner, J. P., and Goehring, B. M.: Quaternary evolution and ice sheet

- 885 history of contrasting landscapes in Uummannaq and Sukkertoppen, western Greenland,
886 Quaternary Science Reviews, 149, 248-258,
887 <https://doi.org/10.1016/j.quascirev.2016.05.033>, 2016.
- 888 Benn, D. and Evans, D. J. A.: *Glaciers and Glaciation*, 2, Routledge,
889 <https://doi.org/10.4324/9780203785010>, 2014.
- 890 Bierman, P. R., Mastro, H. M., Peteet, D. M., Corbett, L. B., Steig, E. J., Halsted, C. T., Caffee,
891 M. M., Hidy, A. J., Balco, G., and Bennike, O.: Plant, insect, and fungi fossils under the
892 center of Greenland's ice sheet are evidence of ice-free times, *Proceedings of the National
893 Academy of Sciences*, 121, <https://doi.org/10.1073/pnas.2407465121>, 2024.
- 894 Bierman, P. R., Marsella, K. A., Patterson, C., Davis, P. T., and Caffee, M.: Mid-Pleistocene
895 cosmogenic minimum-age limits for pre-Wisconsinan glacial surfaces in southwestern
896 Minnesota and southern Baffin Island: a multiple nuclide approach, *Geomorphology*, 27,
897 25-39, [https://doi.org/10.1016/S0169-555X\(98\)00088-9](https://doi.org/10.1016/S0169-555X(98)00088-9), 1999.
- 898 Bierman, P. R., Shakun, J. D., Corbett, L. B., Zimmerman, S. R., and Rood, D. H.: A persistent
899 and dynamic East Greenland Ice Sheet over the past 7.5 million years, *Nature*, 540, 256-
900 260, <https://doi.org/10.1038/nature20147>, 2016.
- 901 Blake, W., Boucherle, M. M., Fredskild, B., Janssens, J. A., and Smol, J. P.: The geomorphological
902 setting, glacial history and Holocene development of Kap Inglefield Sø, Inglefield Land,
903 North-West Greenland, *Meddelelser om Grønland. Geoscience*, 27, 1-42, 1992.
- 904 Briner, J. P. and Swanson, T. W.: Using inherited cosmogenic ³⁶Cl to constrain glacial erosion
905 rates of the Cordilleran ice sheet, *Geology*, 26, 3-6, [https://doi.org/10.1130/0091-
906 7613\(1998\)026<0003:UICCTC>2.3.CO;2](https://doi.org/10.1130/0091-7613(1998)026<0003:UICCTC>2.3.CO;2), 1998.
- 907 Briner, J. P., Miller, G. H., Davis, P. T., and Finkel, R. C.: Cosmogenic radionuclides from fiord
908 landscapes support differential erosion by overriding ice sheets, *Geological Society of
909 America Bulletin*, 118, 406-420, <https://doi.org/10.1130/B25716.1>, 2006.
- 910 Briner, J. P., Miller, G. H., Finkel, R., and Hess, D. P.: Glacial erosion at the fjord onset zone and
911 implications for the organization of ice flow on Baffin Island, Arctic Canada,
912 *Geomorphology*, 97, 126-134, <https://doi.org/10.1016/j.geomorph.2007.02.039>, 2008.
- 913 Briner, J. P., Cuzzone, J. K., Badgley, J. A., Young, N. E., Steig, E. J., Morlighem, M., Schlegel,
914 N.-J., Hakim, G. J., Schaefer, J. M., and Johnson, J. V.: Rate of mass loss from the
915 Greenland Ice Sheet will exceed Holocene values this century, *Nature*, 586, 70-74,
916 <https://doi.org/10.1038/s41586-020-2742-6>, 2020.
- 917 Briner, J. P., Walcott, C. K., Schaefer, J. M., Young, N. E., MacGregor, J. A., Poinar, K., Keisling,
918 B. A., Anandakrishnan, S., Albert, M. R., Kuhl, T., and Boeckmann, G.: Drill-site selection
919 for cosmogenic-nuclide exposure dating of the bed of the Greenland Ice Sheet, *The
920 Cryosphere*, 16, 3933-3948, [10.5194/tc-16-3933-2022](https://doi.org/10.5194/tc-16-3933-2022), 2022.
- 921 Brook, E. J., Nesje, A., Lehman, S. J., Raisbeck, G. M., and Yiou, F. o.: Cosmogenic nuclide
922 exposure ages along a vertical transect in western Norway: implications for the height of
923 the Fennoscandian ice sheet, *Geology*, 24, 207-210, [https://doi.org/10.1130/0091-
924 7613\(1996\)024<0207:CNEAAA>2.3.CO;2](https://doi.org/10.1130/0091-7613(1996)024<0207:CNEAAA>2.3.CO;2), 1996.
- 925 Ceperley, E. G., Marcott, S. A., Reusche, M. M., Barth, A. M., Mix, A. C., Brook, E. J., and Caffee,
926 M.: Widespread early Holocene deglaciation, Washington Land, northwest Greenland,
927 *Quaternary Science Reviews*, 231, 106181,
928 <https://doi.org/10.1016/j.quascirev.2020.106181>, 2020.
- 929 Christ, A. J., Bierman, P. R., Knutz, P. C., Corbett, L. B., Fosdick, J. C., Thomas, E. K., Cowling,



- 930 O. C., Hidy, A. J., and Caffee, M. W.: The northwestern Greenland Ice Sheet during the
931 Early Pleistocene was similar to today, *Geophysical Research Letters*, 47,
932 e2019GL085176, <https://doi.org/10.1029/2019GL085176>, 2020.
- 933 Christ, A. J., Bierman, P. R., Schaefer, J. M., Dahl-Jensen, D., Steffensen, J. P., Corbett, L. B.,
934 Peteet, D. M., Thomas, E. K., Steig, E. J., and Rittenour, T. M.: A multimillion-year-old
935 record of Greenland vegetation and glacial history preserved in sediment beneath 1.4 km
936 of ice at Camp Century, *Proceedings of the National Academy of Sciences*, 118,
937 <https://doi.org/10.1073/pnas.2021442118>, 2021.
- 938 Christ, A. J., Rittenour, T. M., Bierman, P. R., Keisling, B. A., Knutz, P. C., Thomsen, T. B.,
939 Keulen, N., Fosdick, J. C., Hemming, S. R., and Tison, J.-L.: Deglaciation of northwestern
940 Greenland during Marine Isotope Stage 11, *Science*, 381, 330-335,
941 [10.1126/science.ade4248](https://doi.org/10.1126/science.ade4248), 2023.
- 942 Colville, E. J., Carlson, A. E., Beard, B. L., Hatfield, R. G., Stoner, J. S., Reyes, A. V., and Ullman,
943 D. J.: Sr-Nd-Pb Isotope Evidence for Ice-Sheet Presence on Southern Greenland During
944 the Last Interglacial, *Science*, 333, 620-623, [10.1126/science.1204673](https://doi.org/10.1126/science.1204673), 2011.
- 945 Cook, S. J., Swift, D. A., Kirkbride, M. P., Knight, P. G., and Waller, R. I.: The empirical basis
946 for modelling glacial erosion rates, *Nature Communications*, 11, 759, [10.1038/s41467-
947 020-14583-8](https://doi.org/10.1038/s41467-020-14583-8), 2020.
- 948 Corbett, L. B., Bierman, P. R., and Rood, D. H.: Constraining multi-stage exposure-burial
949 scenarios for boulders preserved beneath cold-based glacial ice in Thule, northwest
950 Greenland, *Earth and Planetary Science Letters*, 440, 147-157,
951 <https://doi.org/10.1016/j.epsl.2016.02.004>, 2016a.
- 952 Corbett, L. B., Bierman, P. R., and Rood, D. H.: An approach for optimizing in situ cosmogenic
953 ^{10}Be sample preparation, *Quaternary Geochronology*, 33, 24-34,
954 <https://doi.org/10.1016/j.quageo.2016.02.001>, 2016b.
- 955 Corbett, L. B., Bierman, P. R., Graly, J. A., Neumann, T. A., and Rood, D. H.: Constraining
956 landscape history and glacial erosivity using paired cosmogenic nuclides in Upernavik,
957 northwest Greenland, *Bulletin*, 125, 1539-1553, <https://doi.org/10.1130/B30813.1>, 2013.
- 958 Corbett, L. B., Bierman, P. R., Rood, D. H., Caffee, M. W., Lifton, N. A., and Woodruff, T. E.:
959 Cosmogenic $^{26}\text{Al}/^{10}\text{Be}$ surface production ratio in Greenland, *Geophysical Research
960 Letters*, 44, 1350-1359, <https://doi.org/10.1002/2016GL071276>, 2017.
- 961 Couette, P.-O., Lajeunesse, P., Ghienne, J.-F., Dorschel, B., Gebhardt, C., Hebbeln, D., and
962 Brouard, E.: Evidence for an extensive ice shelf in northern Baffin Bay during the Last
963 Glacial Maximum, *Communications Earth & Environment*, 3, 225,
964 <https://doi.org/10.1038/s43247-022-00559-7>, 2022.
- 965 Cowton, T., Nienow, P., Bartholomew, I., Sole, A., and Mair, D.: Rapid erosion beneath the
966 Greenland ice sheet, *Geology*, 40, 343-346, [10.1130/G32687.1](https://doi.org/10.1130/G32687.1), 2012.
- 967 Cuffey, K. M., Conway, H., Gades, A. M., Hallet, B., Lorrain, R., Severinghaus, J. P., Steig, E. J.,
968 Vaughn, B., and White, J. W. C.: Entrainment at cold glacier beds, *Geology*, 28, 351-354,
969 [https://doi.org/10.1130/0091-7613\(2000\)28<351:EACGB>2.0.CO;2](https://doi.org/10.1130/0091-7613(2000)28<351:EACGB>2.0.CO;2), 2000.
- 970 Cuzzone, J. K., Clark, P. U., Carlson, A. E., Ullman, D. J., Rinterknecht, V. R., Milne, G. A.,
971 Lunkka, J.-P., Wohlfarth, B., Marcott, S. A., and Caffee, M.: Final deglaciation of the
972 Scandinavian Ice Sheet and implications for the Holocene global sea-level budget, *Earth
973 and Planetary Science Letters*, 448, 34-41, <https://doi.org/10.1016/j.epsl.2016.05.019>,
974 2016.
- 975 Daly, R. A.: The geology of the northeast coast of Labrador, *Bulletin of the Museum of*



- 976 Comparative Zoology at Harvard College, Geological Series, 5, 205 - 269, 1902.
- 977 de Vernal, A. and Hillaire-Marcel, C.: Natural variability of Greenland climate, vegetation, and
978 ice volume during the past million years, *Science*, 320, 1622-1625,
979 10.1126/science.1153929, 2008.
- 980 England, J.: Coalescent Greenland and Innuitian ice during the last glacial maximum: revising the
981 Quaternary of the Canadian High Arctic, *Quaternary Science Reviews*, 18, 421-456,
982 [https://doi.org/10.1016/S0277-3791\(98\)00070-5](https://doi.org/10.1016/S0277-3791(98)00070-5), 1999.
- 983 Flint, R. F.: Growth of North American Ice Sheet During the Wisconsin Age, *GSA Bulletin*, 54,
984 325-362, 10.1130/GSAB-54-325, 1943.
- 985 Goelzer, H., Nowicki, S., Payne, A., Larour, E., Seroussi, H., Lipscomb, W. H., Gregory, J., Abe-
986 Ouchi, A., Shepherd, A., Simon, E., Agosta, C., Alexander, P., Aschwanden, A., Barthel,
987 A., Calov, R., Chambers, C., Choi, Y., Cuzzone, J., Dumas, C., Edwards, T., Felikson, D.,
988 Fettweis, X., Golledge, N. R., Greve, R., Humbert, A., Huybrechts, P., Le clec'h, S., Lee,
989 V., Leguy, G., Little, C., Lowry, D. P., Morlighem, M., Nias, I., Quiquet, A., Rückamp,
990 M., Schlegel, N. J., Slater, D. A., Smith, R. S., Straneo, F., Tarasov, L., van de Wal, R.,
991 and van den Broeke, M.: The future sea-level contribution of the Greenland ice sheet: a
992 multi-model ensemble study of ISMIP6, *The Cryosphere*, 14, 3071-3096, 10.5194/tc-14-
993 3071-2020, 2020.
- 994 Goodfellow, B. W., Skelton, A., Martel, S. J., Stroeven, A. P., Jansson, K. N., and Hättestrand, C.:
995 Controls of tor formation, Cairngorm Mountains, Scotland, *Journal of Geophysical*
996 *Research: Earth Surface*, 119, 225-246, <https://doi.org/10.1002/2013JF002862>, 2014.
- 997 Gordon, J. E.: Ice-Scoured Topography and Its Relationships to Bedrock Structure and Ice
998 Movement in Parts of Northern Scotland and West Greenland, *Geografiska Annaler. Series*
999 *A, Physical Geography*, 63, 55-65, <https://doi.org/10.2307/520564>, 1981.
- 1000 Gosse, J. C. and Phillips, F. M.: Terrestrial in situ cosmogenic nuclides: theory and application,
1001 *Quaternary Science Reviews*, 20, 1475-1560, 10.1016/s0277-3791(00)00171-2, 2001.
- 1002 Hall, A. M. and Glasser, N. F.: Reconstructing the basal thermal regime of an ice stream in a
1003 landscape of selective linear erosion: Glen Avon, Cairngorm Mountains, Scotland, *Boreas*,
1004 32, 191-207, <https://doi.org/10.1111/j.1502-3885.2003.tb01437.x>, 2003.
- 1005 Hall, A. M. and Phillips, W. M.: Glacial modification of granite tors in the Cairngorms, Scotland,
1006 *Journal of Quaternary Science*, 21, 811-830, <https://doi.org/10.1002/jqs.1003>, 2006.
- 1007 Hasholt, B., van As, D., Mikkelsen, A. B., Mermild, S. H., and Yde, J. C.: Observed sediment and
1008 solute transport from the Kangerlussuaq sector of the Greenland Ice Sheet (2006–2016),
1009 *Arctic, Antarctic, and Alpine Research*, 50, S100009, 10.1080/15230430.2018.1433789,
1010 2018.
- 1011 Hatfield, R. G., Reyes, A. V., Stoner, J. S., Carlson, A. E., Beard, B. L., Winsor, K., and Welke,
1012 B.: Interglacial responses of the southern Greenland ice sheet over the last 430,000 years
1013 determined using particle-size specific magnetic and isotopic tracers, *Earth and Planetary*
1014 *Science Letters*, 454, 225-236, <https://doi.org/10.1016/j.epsl.2016.09.014>, 2016.
- 1015 Hogan, K. A., Dowdeswell, J. A., and Ó Cofaigh, C.: Glacimarine sedimentary processes and
1016 depositional environments in an embayment fed by West Greenland ice streams, *Marine*
1017 *Geology*, 311-314, 1-16, <https://doi.org/10.1016/j.margeo.2012.04.006>, 2012.
- 1018 Hogan, K. A., Jakobsson, M., Mayer, L., Reilly, B. T., Jennings, A. E., Stoner, J. S., Nielsen, T.,
1019 Andresen, K. J., Nørmark, E., Heirman, K. A., Kamla, E., Jerram, K., Stranne, C., and Mix,
1020 A.: Glacial sedimentation, fluxes and erosion rates associated with ice retreat in Petermann



- 1021 Fjord and Nares Strait, north-west Greenland, *The Cryosphere*, 14, 261-286, 10.5194/tc-
1022 14-261-2020, 2020.
- 1023 Hubbard, A., Bradwell, T., Golledge, N., Hall, A., Patton, H., Sugden, D., Cooper, R., and Stoker,
1024 M.: Dynamic cycles, ice streams and their impact on the extent, chronology and
1025 deglaciation of the British–Irish ice sheet, *Quaternary Science Reviews*, 28, 758-776,
1026 <https://doi.org/10.1016/j.quascirev.2008.12.026>, 2009.
- 1027 Ivy-Ochs, S. and Briner, J. P.: Dating disappearing ice with cosmogenic nuclides, *Elements*, 10,
1028 351-356, <https://doi.org/10.2113/gselements.10.5.351>, 2014.
- 1029 Johnson, J. S., Woodward, J., Nesbitt, I., Winter, K., Campbell, S., Nichols, K. A., Venturelli, R.
1030 A., Braddock, S., Goehring, B. M., Hall, B., Rood, D. H., and Balco, G.: Detecting
1031 Holocene retreat and readvance in the Amundsen Sea sector of Antarctica: assessing the
1032 suitability of sites near Pine Island Glacier for subglacial bedrock drilling, *EGUsphere*,
1033 2024, 1-34, 10.5194/egusphere-2024-1452, 2024.
- 1034 Khan, S. A., Choi, Y., Morlighem, M., Rignot, E., Helm, V., Humbert, A., Mouginot, J., Millan,
1035 R., Kjær, K. H., and Bjørk, A. A.: Extensive inland thinning and speed-up of Northeast
1036 Greenland Ice Stream, *Nature*, 611, 727-732, 10.1038/s41586-022-05301-z, 2022.
- 1037 Knudsen, M. F. and Egholm, D. L.: Constraining Quaternary ice covers and erosion rates using
1038 cosmogenic $^{26}\text{Al}/^{10}\text{Be}$ nuclide concentrations, *Quaternary Science Reviews*, 181, 65-75,
1039 <https://doi.org/10.1016/j.quascirev.2017.12.012>, 2018.
- 1040 Knudsen, M. F., Egholm, D. L., Jacobsen, B. H., Larsen, N. K., Jansen, J. D., Andersen, J. L., and
1041 Linge, H. C.: A multi-nuclide approach to constrain landscape evolution and past erosion
1042 rates in previously glaciated terrains, *Quaternary Geochronology*, 30, 100-113,
1043 <https://doi.org/10.1016/j.quageo.2015.08.004>, 2015.
- 1044 Knutz, P. C., Newton, A. M., Hopper, J. R., Huuse, M., Gregersen, U., Sheldon, E., and Dybkjær,
1045 K.: Eleven phases of Greenland Ice Sheet shelf-edge advance over the past 2.7 million
1046 years, *Nature Geoscience*, 12, 361-368, <https://doi.org/10.1038/s41561-019-0340-8>, 2019.
- 1047 Koerner, R. M.: Ice Core Evidence for Extensive Melting of the Greenland Ice Sheet in the Last
1048 Interglacial, *Science*, 244, 964-968, 10.1126/science.244.4907.964, 1989.
- 1049 Kohl, C. P. and Nishiizumi, K.: Chemical isolation of quartz for measurement of in-situ-produced
1050 cosmogenic nuclides, *Geochimica et Cosmochimica Acta*, 56, 3583-3587,
1051 [https://doi.org/10.1016/0016-7037\(92\)90401-4](https://doi.org/10.1016/0016-7037(92)90401-4), 1992.
- 1052 Kokfelt, T. F., Willerslev, E., Bjerager, M., Heijboer, T., Keulen, N., Larsen, L. M., Pedersen, C.
1053 B., Pedersen, M., Svennevig, K., Sønderholm, M., Walentin, K. T., and Weng, W. L.:
1054 Seamless digital 1:500 000 scale geological map of Greenland, version 2.0 (V1), GEUS
1055 Dataverse [dataset], doi:10.22008/FK2/FWX5ET, 2023.
- 1056 Koppes, M., Hallet, B., Rignot, E., Mouginot, J., Wellner, J. S., and Boldt, K.: Observed latitudinal
1057 variations in erosion as a function of glacier dynamics, *Nature*, 526, 100-103,
1058 10.1038/nature15385, 2015.
- 1059 Koppes, M. N. and Montgomery, D. R.: The relative efficacy of fluvial and glacial erosion over
1060 modern to orogenic timescales, *Nature Geoscience*, 2, 644-647, 10.1038/ngeo616, 2009.
- 1061 Korschinek, G., Bergmaier, A., Faestermann, T., Gerstmann, U. C., Knie, K., Rugel, G., Wallner,
1062 A., Dillmann, I., Dollinger, G., von Gostomski, C. L., Kossert, K., Maiti, M., Poutivtsev,
1063 M., and Remmert, A.: A new value for the half-life of ^{10}Be by Heavy-Ion Elastic Recoil
1064 Detection and liquid scintillation counting, *Nuclear Instruments and Methods in Physics
1065 Research Section B: Beam Interactions with Materials and Atoms*, 268, 187-191,
1066 <https://doi.org/10.1016/j.nimb.2009.09.020>, 2010.



- 1067 Korsgaard, N. J., Nuth, C., Khan, S. A., Kjeldsen, K. K., Bjørk, A. A., Schomacker, A., and Kjær,
1068 K. H.: Digital elevation model and orthophotographs of Greenland based on aerial
1069 photographs from 1978–1987, *Scientific Data*, 3, 1–15,
1070 <https://doi.org/10.1038/sdata.2016.32>, 2016.
- 1071 Krabbendam, M. and Bradwell, T.: Quaternary evolution of glaciated gneiss terrains: pre-glacial
1072 weathering vs. glacial erosion, *Quaternary Science Reviews*, 95, 20–42,
1073 <https://doi.org/10.1016/j.quascirev.2014.03.013>, 2014.
- 1074 Lal, D.: Cosmic ray labeling of erosion surfaces: in situ nuclide production rates and erosion
1075 models, *Earth and Planetary Science Letters*, 104, 424–439, [https://doi.org/10.1016/0012-821X\(91\)90220-C](https://doi.org/10.1016/0012-821X(91)90220-C), 1991.
- 1077 LeBlanc, D. E., Shakun, J. D., Corbett, L. B., Bierman, P. R., Caffee, M. W., and Hidy, A. J.:
1078 Laurentide Ice Sheet persistence during Pleistocene interglacials, *Geology*, 51, 496–499,
1079 [10.1130/G50820.1](https://doi.org/10.1130/G50820.1), 2023.
- 1080 Lisiecki, L. E. and Raymo, M. E.: A Pliocene-Pleistocene stack of 57 globally distributed benthic
1081 $\delta^{18}\text{O}$ records, *Paleoceanography*, 20, <https://doi.org/10.1029/2004PA001071>, 2005.
- 1082 MacGregor, J. A., Chu, W., Colgan, W. T., Fahnestock, M. A., Felikson, D., Karlsson, N. B.,
1083 Nowicki, S. M. J., and Studinger, M.: GBaTSv2: A revised synthesis of the likely basal
1084 thermal state of the Greenland Ice Sheet, *The Cryosphere Discuss.*, 2022, 1–25, [10.5194/tc-2022-40](https://doi.org/10.5194/tc-2022-40), 2022.
- 1086 Margold, M., Stokes, C. R., and Clark, C. D.: Ice streams in the Laurentide Ice Sheet:
1087 Identification, characteristics and comparison to modern ice sheets, *Earth-Science
1088 Reviews*, 143, 117–146, <https://doi.org/10.1016/j.earscirev.2015.01.011>, 2015.
- 1089 Margold, M., Stokes, C. R., and Clark, C. D.: Reconciling records of ice streaming and ice margin
1090 retreat to produce a palaeogeographic reconstruction of the deglaciation of the Laurentide
1091 Ice Sheet, *Quaternary Science Reviews*, 189, 1–30,
1092 <https://doi.org/10.1016/j.quascirev.2018.03.013>, 2018.
- 1093 Margreth, A., Gosse, J. C., and Dyke, A. S.: Quantification of subaerial and episodic subglacial
1094 erosion rates on high latitude upland plateaus: Cumberland Peninsula, Baffin Island, Arctic
1095 Canada, *Quaternary Science Reviews*, 133, 108–129,
1096 <https://doi.org/10.1016/j.quascirev.2015.12.017>, 2016.
- 1097 Marrero, S. M., Hein, A. S., Naylor, M., Attal, M., Shanks, R., Winter, K., Woodward, J., Dunning,
1098 S., Westoby, M., and Sugden, D.: Controls on subaerial erosion rates in Antarctica, *Earth
1099 and Planetary Science Letters*, 501, 56–66, <https://doi.org/10.1016/j.epsl.2018.08.018>,
1100 2018.
- 1101 Mason, O. K.: Beach ridge geomorphology at Cape Grinnell, northern Greenland: a less icy Arctic
1102 in the mid-Holocene, *Geografisk Tidsskrift-Danish Journal of Geography*, 110, 337–355,
1103 <https://doi.org/10.1080/00167223.2010.10669515>, 2010.
- 1104 Miller, G. H., Briner, J. P., Lifton, N. A., and Finkel, R. C.: Limited ice-sheet erosion and complex
1105 exposure histories derived from in situ cosmogenic ^{10}Be , ^{26}Al , and ^{14}C on Baffin Island,
1106 Arctic Canada, *Quaternary Geochronology*, 1, 74–85,
1107 <https://doi.org/10.1016/j.quageo.2006.06.011>, 2006.
- 1108 Mouginot, J., Rignot, E., Scheuchl, B., Fenty, I., Khazendar, A., Morlighem, M., Buzzi, A., and
1109 Paden, J.: Fast retreat of Zachariæ Isstrøm, northeast Greenland, *Science*, 350, 1357–1361,
1110 [10.1126/science.aac7111](https://doi.org/10.1126/science.aac7111), 2015.
- 1111 Nichols, R. L.: Geomorphology of Inglefield land, north Greenland, *Meddelelser om Grønland*,
1112 188, 3–105, 1969.



- 1113 Nishiizumi, K.: Preparation of ^{26}Al AMS standards, *Nuclear Instruments and Methods in Physics*
1114 *Research Section B: Beam Interactions with Materials and Atoms*, 223-224, 388-392,
1115 <https://doi.org/10.1016/j.nimb.2004.04.075>, 2004.
- 1116 Nishiizumi, K., Imamura, M., Caffee, M. W., Southon, J. R., Finkel, R. C., and McAninch, J.:
1117 Absolute calibration of ^{10}Be AMS standards, *Nuclear Instruments and Methods in Physics*
1118 *Research Section B: Beam Interactions with Materials and Atoms*, 258, 403-413,
1119 <https://doi.org/10.1016/j.nimb.2007.01.297>, 2007.
- 1120 Patton, H., Hubbard, A., Andreassen, K., Auriac, A., Whitehouse, P. L., Stroeven, A. P.,
1121 Shackleton, C., Winsborrow, M., Heyman, J., and Hall, A. M.: Deglaciation of the Eurasian
1122 ice sheet complex, *Quaternary Science Reviews*, 169, 148-172,
1123 <https://doi.org/10.1016/j.quascirev.2017.05.019>, 2017.
- 1124 Phillips, W. M., Hall, A. M., Mottram, R., Fifield, L. K., and Sugden, D. E.: Cosmogenic ^{10}Be
1125 and ^{26}Al exposure ages of tors and erratics, Cairngorm Mountains, Scotland: Timescales
1126 for the development of a classic landscape of selective linear glacial erosion,
1127 *Geomorphology*, 73, 222-245, <https://doi.org/10.1016/j.geomorph.2005.06.009>, 2006.
- 1128 Portenga, E. W. and Bierman, P. R.: Understanding Earth's eroding surface with ^{10}Be , *GSA*
1129 *Today*, 21, 6, 10.1130/G111A.1, 2011.
- 1130 Reyes, A. V., Carlson, A. E., Beard, B. L., Hatfield, R. G., Stoner, J. S., Winsor, K., Welke, B.,
1131 and Ullman, D. J.: South Greenland ice-sheet collapse during marine isotope stage 11,
1132 *Nature*, 510, 525-528, <https://doi.org/10.1038/nature13456>, 2014.
- 1133 Roberts, D. H., Rea, B. R., Lane, T. P., Schnabel, C., and Rodés, A.: New constraints on Greenland
1134 ice sheet dynamics during the last glacial cycle: evidence from the Uummannaq ice stream
1135 system, *Journal of Geophysical Research: Earth Surface*, 118, 519-541,
1136 <https://doi.org/10.1002/jgrf.20032>, 2013.
- 1137 Sbarra, C. M., Briner, J. P., Graham, B. L., Poinar, K., Thomas, E. K., and Young, N. E.: Evidence
1138 for a more extensive Greenland Ice Sheet in southwestern Greenland during the Last
1139 Glacial Maximum, *Geosphere*, <https://doi.org/10.1130/GES02432.1>, 2022.
- 1140 Schaefer, J. M., Finkel, R. C., Balco, G., Alley, R. B., Caffee, M. W., Briner, J. P., Young, N. E.,
1141 Gow, A. J., and Schwartz, R.: Greenland was nearly ice-free for extended periods during
1142 the Pleistocene, *Nature*, 540, 252-255, <https://doi.org/10.1038/nature20146>, 2016.
- 1143 Skov, D. S., Andersen, J. L., Olsen, J., Jacobsen, B. H., Knudsen, M. F., Jansen, J. D., Larsen, N.
1144 K., and Egholm, D. L.: Constraints from cosmogenic nuclides on the glaciation and erosion
1145 history of Dove Bugt, northeast Greenland, *GSA Bulletin*, 132, 2282-2294,
1146 10.1130/B35410.1, 2020.
- 1147 Skyttä, P., Nordbäck, N., Ojala, A., Putkinen, N., Aaltonen, I., Engström, J., Mattila, J., and
1148 Ovaskainen, N.: The interplay of bedrock fractures and glacial erosion in defining the
1149 present-day land surface topography in mesoscopically isotropic crystalline rocks, *Earth*
1150 *Surface Processes and Landforms*, <https://doi.org/10.1002/esp.5596>, 2023.
- 1151 Søndergaard, A. S., Larsen, N. K., Steinemann, O., Olsen, J., Funder, S., Egholm, D. L., and Kjær,
1152 K. H.: Glacial history of Inglefield Land, north Greenland from combined in situ ^{10}Be
1153 and ^{14}C exposure dating, *Climate of the Past*, 16, 1999-2015, [https://doi.org/10.5194/cp-](https://doi.org/10.5194/cp-16-1999-2020)
1154 16-1999-2020, 2020.
- 1155 Spector, P., Stone, J., Pollard, D., Hillebrand, T., Lewis, C., and Gombiner, J.: West Antarctic sites
1156 for subglacial drilling to test for past ice-sheet collapse, *The Cryosphere*, 12, 2741-2757,
1157 <https://doi.org/10.5194/tc-12-2741-2018>, 2018.
- 1158 Stone, J. O.: Air pressure and cosmogenic isotope production, *Journal of Geophysical Research:*



- 1159 Solid Earth, 105, 23753-23759, <https://doi.org/10.1029/2000JB900181>, 2000.
- 1160 Strunk, A., Knudsen, M. F., Egholm, D. L., Jansen, J. D., Levy, L. B., Jacobsen, B. H., and Larsen,
1161 N. K.: One million years of glaciation and denudation history in west Greenland, Nature
1162 communications, 8, 1-8, <https://doi.org/10.1038/ncomms14199>, 2017.
- 1163 Sugden, D. E.: Landscapes of glacial erosion in Greenland and their relationship to ice,
1164 topographic and bedrock conditions, Institute of British Geographers Special Publication,
1165 7, 177-195, 1974.
- 1166 Sugden, D. E.: Glacial Erosion by the Laurentide Ice Sheet, Journal of Glaciology, 20, 367-391,
1167 10.3189/S0022143000013915, 1978.
- 1168 Sugden, D. E., Balco, G., Cowdery, S. G., Stone, J. O., and Sass, L. C.: Selective glacial erosion
1169 and weathering zones in the coastal mountains of Marie Byrd Land, Antarctica,
1170 Geomorphology, 67, 317-334, <https://doi.org/10.1016/j.geomorph.2004.10.007>, 2005.
- 1171 Syvitski, J. P. M., Andrews, J. T., and Dowdeswell, J. A.: Sediment deposition in an iceberg-
1172 dominated glacimarine environment, East Greenland: basin fill implications, Global and
1173 Planetary Change, 12, 251-270, [https://doi.org/10.1016/0921-8181\(95\)00023-2](https://doi.org/10.1016/0921-8181(95)00023-2), 1996.
- 1174 Ugelvig, S. V. and Egholm, D. L.: The influence of basal-ice debris on patterns and rates of glacial
1175 erosion, Earth and Planetary Science Letters, 490, 110-121,
1176 <https://doi.org/10.1016/j.epsl.2018.03.022>, 2018.
- 1177 Young, N. E., Schaefer, J. M., Briner, J. P., and Goehring, B. M.: A ^{10}Be production-rate
1178 calibration for the Arctic, Journal of Quaternary Science, 28, 515-526,
1179 <https://doi.org/10.1002/jqs.2642>, 2013.
- 1180 Young, N. E., Lesnek, A. J., Cuzzone, J. K., Briner, J. P., Badgley, J. A., Balter-Kennedy, A.,
1181 Graham, B. L., Cluett, A., Lamp, J. L., Schwartz, R., Tuna, T., Bard, E., Caffee, M. W.,
1182 Zimmerman, S. R. H., and Schaefer, J. M.: In situ cosmogenic ^{10}Be - ^{14}C - ^{26}Al
1183 measurements from recently deglaciated bedrock as a new tool to decipher changes in
1184 Greenland Ice Sheet size, Clim. Past, 17, 419-450, 10.5194/cp-17-419-2021, 2021.
- 1185
- 1186